Lattice Boltzmann very large eddy simulations of a turbulent flow over covered and uncovered cavities

Physics of Fluids

Lattice Boltzmann very large eddy simulations of a turbulent flow over covered and uncovered cavities

Cite as: Phys. Fluids **34**, 105120 (2022); https://doi.org/10.1063/5.0100001
Submitted: 20 May 2022 • Accepted: 07 September 2022 • Published Online: 13 October 2022

Published open access through an agreement with Technische Universiteit Delft Faculteit Luchtvaart- en Ruimtevaarttechniek

Hugo F. Mourão Bento, Colin P. VanDercreek, Francesco Avallone, et al.

Physics of Fluids ARTICLE scitation.org/journal/phf

Lattice Boltzmann very large eddy simulations of a turbulent flow over covered and uncovered cavities

Cite as: Phys. Fluids 34, 105120 (2022); doi: 10.1063/5.0100001
Submitted: 20 May 2022 · Accepted: 7 September 2022 ·
Published Online: 13 October 2022

Hugo F. Mourão Bento,[a] Colin P. VanDercreek,[a] Francesco Avallone, Daniele Ragni, and Mirjam Snellen

AFFILIATIONS

Faculty of Aerospace Engineering, Delft University of Technology, Kluyverweg 1, Delft 2629HS, The Netherlands

[a]Authors to whom correspondence should be addressed: H.F.MouraoBento@tudelft.nl and C.P.vanDercreek@tudelft.nl

ABSTRACT

Microphone measurements in a closed test section wind tunnel are affected by turbulent boundary layer (TBL) pressure fluctuations. These fluctuations are mitigated by placing the microphones at the bottom of cavities, usually covered with a thin, acoustically transparent material. Prior experiments showed that the cavity geometry affects the propagation of TBL pressure fluctuations toward the bottom. However, the relationship between the cavity geometry and the flowfield within the cavity is not well understood. Therefore, a very large-eddy simulation was performed using the lattice Boltzmann method. A cylindrical, a countersunk and a conical cavity are simulated with and without a fine wire-cloth cover, which is modeled as a porous medium governed by Darcy's law. Adding a countersink to an uncovered cylindrical cavity is found to mitigate the transport of turbulent structures across the bottom by shifting the recirculation pattern away from the cavity bottom. Covering the cavities nearly eliminates this source of hydrodynamic pressure fluctuations. The eddies within the boundary layer, which convect over the cover, generate a primarily acoustic pressure field inside the cavities and thus suggesting that the pressure fluctuations within covered cavities can be modeled acoustically. As the cavity diameter increases compared to the eddies' integral length scale, the amount of energy in the cut-off modes increases with respect to the cut-on modes. Since cut-off modes decay as they propagate into the cavity, more attenuation is seen. The results are in agreement with experimental evidence.

I. INTRODUCTION

The signal-to-noise ratio (SNR) of flush mounted microphone array measurements in closed test section wind tunnels is reduced by the presence of a turbulent boundary layer (TBL) over the tunnel walls. The amount of SNR reduction by the TBL pressure fluctuations can be minimized, relative to a microphone mounted flush to the tunnel wall, by placing microphones within cavities. Research on flow over cavities has focused primarily on radiated noise from the interaction of the shear layer over rectangular cavities. The research presented in this article focuses on how the pressure fluctuations at the bottom of axisymmetric cavities, resulting from turbulent flow, are affected by cavity geometry.

Pressure fluctuations within cavities are produced by several mechanisms, which include the Rossiter feedback loop, turbulence within the shear layer, and the transport and production of turbulence due to recirculation within the cavity. The Rossiter feedback loop[1–3] is a self-sustaining noise generation mechanism produced by Kelvin–Helmholtz type vortices[4] shed from the cavity upstream edge. When the vortices impinge on the downstream wall, pressure waves are produced[5,6] that perturb the shear layer, which further produces vortex shedding. The feedback loop is characteristic of cavities exposed to a boundary layer with relatively large momentum thickness, with respect to the cavity aperture.[7] For rectangular cavities, these vortices extend along the spanwise length of the cavity[8] and their impingement produces tonal peaks in the far-field noise spectra. Axisymmetric cavities exhibit similar behavior;[9] however, the vortices shed by cylindrical cavities are affected by the curved cavity edge.[10] Specifically, the vortex spanwise length is smaller than the cavity diameter and they are shed from multiple spanwise locations along the upstream edge.[11] This results in a weaker and broader spectral peak compared to rectangular cavities.[2]

In addition to the shed vortices, the shear layer contains randomly fluctuating turbulence, which produces pressure fluctuations that propagate into the cavity, referred to as turbulent rumble.[12] The strength of these fluctuations increases from the leading edge toward

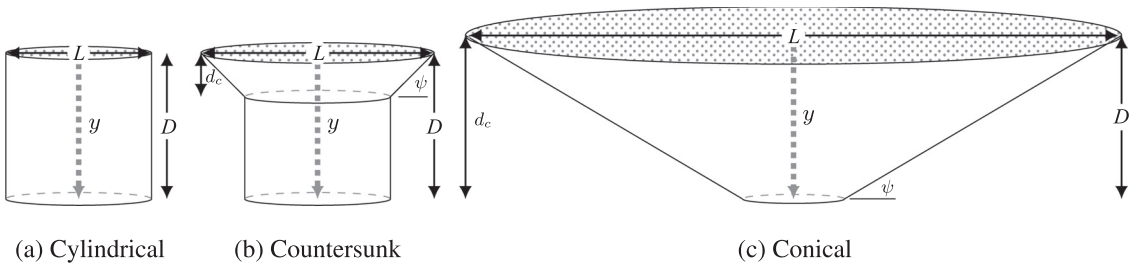

FIG. 1. Simulated cavity geometries: (a) cylindrical, (b) countersunk, and (c) conical.

the downstream edge as shown by particle-image-velocimetry (PIV) measurements.[11] The shape of the upstream edge influences the stability of the shear layer because non-sharp edges can cause the location of the separation point to vary in time,[13] which affects the amplitude of the turbulent rumble.[14]

Recirculation of the fluid due to the flow entering the cavities results in the presence of turbulent pressure fluctuations at the cavity bottom.[15] For deep cylindrical cavities, the recirculating flow is symmetric with respect to the cavity centerline.[16] The recirculation patterns within these deep cavities are stable, in contrast to shallower cavities, which feature unsteady and asymmetric recirculation patterns.[17,18] The recirculating flow causes strong wall shear, which generates fluctuations as high as ≈35% of the local velocity.[15] These velocity fluctuations are highest between the downstream bottom corner and the cavity center, along the cavity centerline.[9,18] This region of increased turbulence corresponds to a region of higher static pressure.[18]

These phenomena can excite acoustic cavity modes that radiate acoustic noise into the far-field. For example, the Rossiter mode produces strong acoustic tones if they are locked on with an acoustic cavity mode.[19–21] Acoustic depth modes are also excited by the turbulent rumble as well as the acoustic energy produced by the shed vortices.[5] For the deep cavities, defined as $L/D \leq 1$, acoustic depth modes are the most significant.[22,23]

A previous study[24] characterized how axisymmetric cavities with different diameters, depths, countersink depths, coverings, and wall angles affect the pressure fluctuations, produced by the TBL, at a microphone placed at the bottom. Cavities with angled walls, e.g., cavities with a countersink, reduce the TBL noise more than cylindrical cavities.[24] Additionally, covering the cavity with Kevlar[25] or finely woven stainless-steel cloth[24] reduces the amplitude of pressure fluctuations at the microphone location by 10–20 dB.[25] This reduction is assumed to be caused by the cover preventing flow into the cavity, reducing the hydrodynamic source of pressure fluctuations. Previous experiments, conducted as part of this project,[26,27] have measured the effect that cylindrical cavities, with and without a countersink, and conical cavities, as illustrated in Fig. 1, have on the attenuation of pressure fluctuations due to the TBL. When these three cavities are uncovered, the countersunk cavity attenuates the TBL pressure fluctuations the most, followed by the cylindrical one. The conical cavity performs the worst as the pressure spectra at the bottom are higher than the spectra measured by a flush mounted microphone. Covering the cavities alters this trend: the conical cavity attenuates the pressure spectra at the bottom more than the countersunk and cylindrical cavities. However, better insight into the relationship between the mechanisms that produce pressure fluctuations and cavity geometry is needed to further optimize the geometry. Currently, there is a lack of literature describing the physical mechanisms that affect the amplitude of pressure fluctuations at the bottom of axisymmetric microphone cavities, especially for covered cavities.

The objective of this work is to understand the effect of aperture size, different countersink depth ratios, i.e., the ratio between the cavity depth and the countersink depth, wall angles, and the presence of a covering have on the recirculation within the cavities, vortex shedding, and turbulence generation, which contribute to the pressure fluctuations at the cavity bottoms. Given the size and geometry of the cavities, non-intrusive velocity-field measurements to identify and study the flow phenomena within the cavity are challenging. Hence, a very-large eddy simulation (VLES) was performed using a lattice Boltzmann method (LBM) solver, SIMULIA PowerFLOW. This article is organized as follows: Sec. II describes the cavity geometries and the PowerFLOW simulation parameters, the validation measurements, and the post-processing used in this analysis. Section III discusses the simulation verification and validation. Section IV analyses the flowfield and pressure field in the time-averaged, instantaneous, and wavenumber domains. Section V evaluates the porous covering's effect on the flowfield in the time-averaged, frequency, and wavenumber domains. Additionally, the effect of geometry on the propagation of the pressure fluctuations is analyzed. Finally, Sec. VI summarizes the major findings of this article.

II. METHODOLOGY

A. Computational setup

1. Geometry

The following axisymmetric cavity geometries are studied: a cylindrical cavity with and without a countersink, and a conical cavity. These three cavities and their geometric parameters are shown in Fig. 1. These cavity geometries were chosen because they are representative of the cavities commonly used in wind tunnel experiments.[26,27] Each cavity is investigated with and without a stainless-steel cloth cover. The following cavity geometric parameters are defined in Table I: aperture size (L), depth (D), countersink depth ratio (d_c/D),

TABLE I. Cavity geometric parameters.

Cavity	L, cm	D, cm	d_c/D	L/θ	ψ
Cylindrical	1.0	1.0	0.0	2.5	90°
Countersunk	1.6	1.0	0.3	4.1	45°
Conical	4.5	1.23	1.0	11.4	30°

ratio of aperture size to BL momentum thickness (L/θ), and wall angle (ψ). For the cylindrical cavity, the aperture diameter is $L = 2.5\theta$, where θ is the momentum thickness of the incoming boundary layer (described in Sec. III B). The relatively small L/θ is expected to avoid the cavity wake mode described in Ref. 7. For an array of microphone cavities, the cavity wake mode would likely cause the downstream cavities to experience a highly turbulent incoming flow.

2. Solver setup

The simulations are performed with the commercial software SIMULIA PowerFLOW 6-2019, which is based on the lattice Boltzmann method, coupled with a VLES approach. The LBM is based on kinetic models which take into account mesoscopic processes in order to obtain reliable continuum flow quantities, in agreement with the macroscopic dynamics of a fluid. PowerFLOW solves the LBM equation on a lattice, i.e., a Cartesian grid. The lattice consists of cubic cells, referred to as voxels, with 19 degrees of freedom. The LBM–VLES solver considers a discrete form of the lattice Boltzmann equation, which can be written as follows:[28]

$$F_i(\boldsymbol{x} + V_i\Delta t, t + \Delta t) - F_i(\boldsymbol{x}, t) = C_i(\boldsymbol{x}, t), \tag{1}$$

where $\boldsymbol{x}$ and t are the space and time coordinates. F_i is the particle distribution function along the ith lattice direction, and V_i is the discrete particle velocity in the same direction. The collision operator, C_i, is based on the Bhatnagar–Gross–Krook kinetic model,[29] and is defined as follows:

$$C_i = -\frac{\Delta t}{\tau}\left[F_i(\boldsymbol{x}, t) - F_i^{eq}(\boldsymbol{x}, t)\right], \tag{2}$$

where $F_i^{eq}(\boldsymbol{x}, t)$ is the equilibrium distribution function, estimated from statistical physics considerations.[30] τ is the viscosity-dependent, collision relaxation time.[30]

In an LBM–VLES approach, the small scales of turbulence are accounted for by correcting the relaxation time used in the calculation of the collision term. Following the work of Ref. 31, a two-equation $k-\varepsilon$ renormalization group is used to compute a turbulent relaxation time that is added to the viscous relaxation time, such that the effective relaxation time reads as follows:

$$\tau_{\text{eff}} = \tau + C_\mu \frac{k^2/\varepsilon}{(1+\eta^2)^{0.5}}, \tag{3}$$

where k is the turbulent kinetic energy (TKE) and ϵ is the rate of dissipation of turbulent kinetic energy. $C_\mu = 0.09$ and η are a combination of the local strain, local vorticity, and local helicity. The term η mitigates the sub-grid scale viscosity in the presence of large resolved vortical structures. The solver can realistically represent boundary layer profiles at large Reynolds numbers without resolving the flow in the viscous sub-layer of the boundary layer by using a pressure gradient-dependent wall model.[30]

3. Porous model

The covered cavities are covered with a finely woven stainless-steel cloth, which has a wire diameter of 2.6×10^{-3} mm and a density of 200 wires per cm^2. This cloth was used in prior cavity experiments[27] and for this work is modeled as a porous medium, as proposed in Ref. 32. This model uses the experimentally measured viscous and inertial resistivities, R_v and R_i, of the cloth, as described in Sec. II B, to impose Darcy's law in the porous medium. Literature[28] suggests this simulation approach is capable of predicting the influence of a porous region on a grazing turbulent boundary layer. This provides confidence that the porous model can be used to simulate the current unsteady problem. Darcy's law relates the pressure drop across the porous medium, Δp, to the Darcy's velocity, v_d, according to[28]

$$\frac{\Delta p}{t} = R_v \boldsymbol{v_d} + \rho R_i \boldsymbol{v_d}^2, \tag{4}$$

where t is the thickness of the porous medium and ρ is the density of air. In order to have sufficient cells inside the porous region, so that the solver can simulate the relationship between flow velocity and pressure gradient, the thickness of the porous medium in the simulation is approximately three times larger than the thickness of the physical stainless-steel cloth (exact dimensions in Table V in Appendix). To account for this, the resistivity values R_v and R_i were multiplied by the ratio between the thickness of the measured sample and the thickness of the porous medium in the simulation. A permeability tube simulation was performed (with the numerical setup described in Ref. 33) to confirm that the porous medium with increased thickness, and corrected R_v and R_i, matches the experimental $\Delta p/t$.

4. Domain and operating conditions

The computational domain for the circular and countersunk cavities is shown in Fig. 2. The bottom of the domain is a flat plate with a no-slip condition at the wall. The cavity, which also contains no-slip walls, is placed at the origin of the domain, i.e., at the center with respect to the length of the streamwise and spanwise domain lengths. This center is located 150 cm (150 $L_{\text{Cylindrical}}$) downstream of the inlet. At the inlet, a turbulent boundary layer mean velocity profile, based on experimental measurements from Ref. 27, is imposed ($\delta_{99} = 1.4$ cm at the inlet). A zigzag trip is placed downstream of the inlet, introducing coherent vortices in the boundary layer. The (no-slip) zigzag trip is 0.16 cm high and has 0.427 cm length, 0.427 cm pitch and 90 dB of top angle (dimensions as defined in Ref. 34). The boundary layer downstream of the zigzag trip is turbulent. The free-stream velocity, U_∞, is set at 32 m s^{-1}, which is within the U_∞ range of interest for closed wind tunnel wind turbine airfoil aeroacoustic testing.[35] As shown in Fig. 2, the sides of the domain have a periodic boundary condition (BC). The span of the domain was chosen to minimize the influence of the boundaries on the cavity flowfield. For the cylindrical and countersunk cavities, a value of $3.2L_{\text{Countersunk}}$ was selected. The distance from the cavity to the boundaries is larger than the spanwise coherence length of the pressure fluctuations in the boundary layer, which is typically on the order of the boundary layer displacement thickness.[36] The span of the domain for the conical cavity simulations is increased to $1.7L_{\text{Conical}}$ (covered configuration) and $2.6L_{\text{Conical}}$ (uncovered). The top of the domain is bounded by a free-slip wall and is located 136 cm above the bottom wall (flatplate). The outlet of the domain imposes an ambient static pressure (sea level pressure). Figure 2 shows a representation of the variable resolution (VR) regions in the computational domain. The VR regions specify the amount of lattice refinement, where VR0 is the finest and VR5 the coarsest, for the uncovered cavities. The VR regions are similar for the

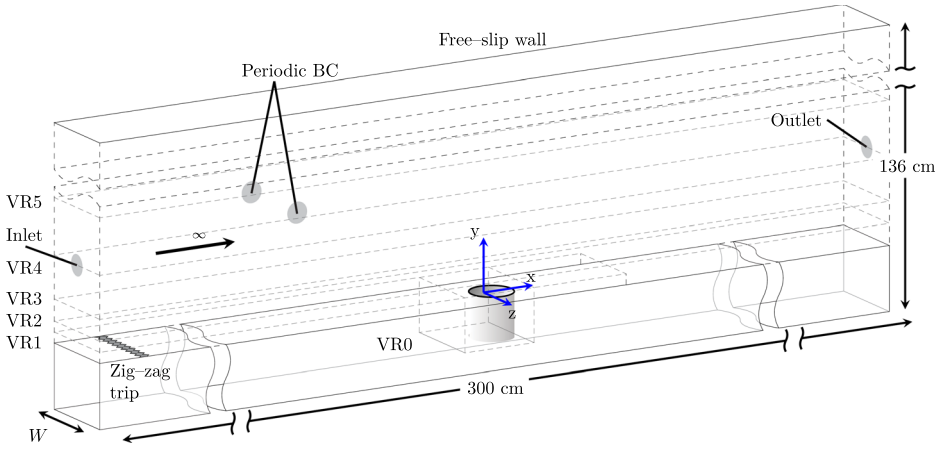

FIG. 2. Representation of the computational domain.

covered cavity simulations, which have an additional finer resolution region around the location of the cloth cover, as shown in Fig. 3. Appendix (Table V) contains additional details on the domain and VR dimensions.

B. Experimental setup

1. Cavity pressure measurements

The experimental data used for validation were measured in the TU Delft A-Tunnel using the same procedure as described in Ref. 27. This tunnel is a vertical open jet wind tunnel located within an anechoic chamber.[37] The cavities in Fig. 1 were made of polycarbonate and mounted on a plate flush with the exit nozzle. The cavities were placed 76 cm downstream of the tunnel nozzle exit. Two plates with dimensions of $110 \times 40\ \text{cm}^2$ were used. One was uncovered and the other was covered with a 200 threads per cm^2 (#500) stainless-steel cloth. A flush-mounted microphone was placed 3.2 cm downstream with a spanwise offset of 4.5 cm. The three cavities were tested in each plate. The tunnel flow speed was $32\ \text{m s}^{-1}$ at the cavity's location.

Sonion 8010T omni-directional MEMS microphones were used to measure the pressure fluctuations. This microphone has an outer diameter of 2.5 mm and a transducer diameter of 0.05 mm. The microphones were center mounted on a 7 mm diameter holder in order to fit securely within the cavities. All the microphones were calibrated individually using a G.R.A.S. 42AG pistonphone following the guidelines of Mueller.[38] The microphones have a flat frequency response within ±1 dB from 100 Hz to 10 kHz. The data acquisition system consists of a National Instruments (NIs) NI9215 analog input module mounted in the NI cDAQ-9178 CompactDAQ with 16-bit resolution. The sampling frequency of the measurements was 51.2 kHz, and the data were recorded for 45 s.

2. Stainless-steel cloth permeability measurements

A 7.5×10^{-3} cm-thick stainless-steel cloth sample was installed in a permeability tube to determine the viscous and inertial resistance of the cloth. The pressure drop, Δp, across the sample as well as the volumetric flow, Q, through the sample were measured. The Darcy velocity, v_d, is calculated as follows: $v_d = Q/A$, where A is the cross-sectional area of the tube. The measured Δp and v_d are fit to the

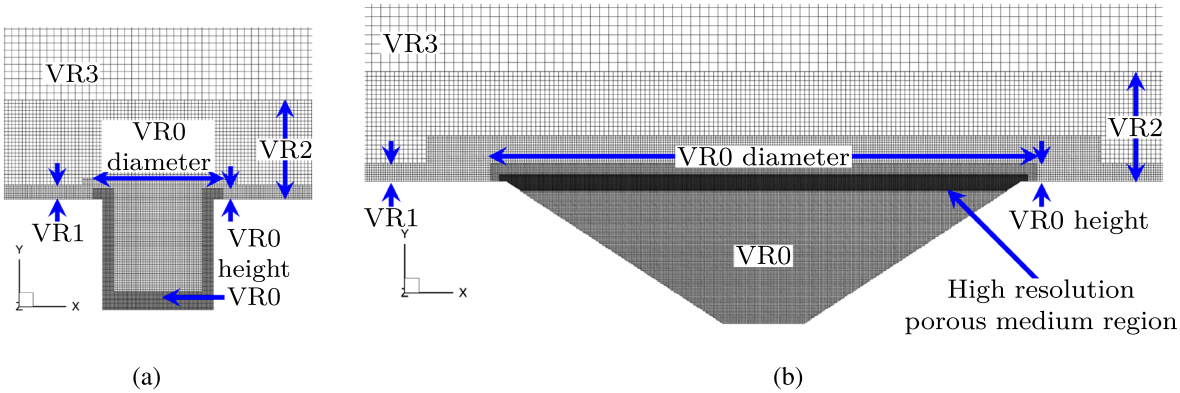

FIG. 3. Grid topology at the cavities location: (a) uncovered cylindrical cavity and (b) covered conical cavity.

TABLE II. Experimentally measured stainless-steel cloth permeability characteristics with 95% confidence intervals.

K, m^{-2}	C, m^{-1}	R_v, s^{-1}
3.0×10^{-11} $\pm 1.0 \times 10^{-14}$	3.1×10^{4} $\pm 1.6 \times 10^{5}$	5.0×10^{5} $\pm 1.7 \times 10^{2}$

Hazen–Dupuit–Darcy equation [Eq. (4)] using a least squares fit method[39,40] to determine the permeability, $K = \frac{\mu}{R_v}$, and the form drag coefficient, $C = R_i$, where μ is the viscosity of air. Further details on the permeability tube can be found in Refs. 39 and 40.

The cloth sample was mounted between two $9.0 \times 9.0\,\text{cm}^2$ polycarbonate plates each with 5.1 cm diameter holes at the center. Epoxy was applied to one polycarbonate plate and the cloth was then stretched across the plate so that the material was tensioned across the opening. Pressure taps within the tube are located 5 cm upstream and downstream of the sample.[39] The static pressure was measured with a Mensor 2101 differential pressure sensor, which has a range of 1.2–15 kPa and an accuracy of 2 Pa. The volumetric flow rate was controlled using an Aventics pressure regulator and measured by a TSI4040 volumetric flowmeter. The Darcy's velocity flow range in the tube is between 0 and $2.5\,\text{m s}^{-1}$, and the permeability tube has a cross-sectional area of $2.04 \times 10^{-3}\,\text{m}^2$. The flowmeter has an accuracy of 2%.[39,40] The pressure drop was measured at 22 discrete velocities ranging from 0 to $2.2\,\text{m s}^{-1}$. The resulting permeability K, the form drag coefficient C, inertial resistance, and viscous resistance are provided in Table II.

C. Post-processing methods

1. Spectral analysis

The power spectral density (PSD) of the pressure field at a given point within the cavity, P_{xx}, was calculated using the Welch's method.[38] A Hanning window was used with 50% overlap when computing the spectra. For all cavities, with and without a covering, a window size of 512 samples was used. The PSD was converted to a decibel scale with a reference pressure of 2×10^{-5} Pa.

2. Wavenumber analysis

A wavenumber-frequency spectral analysis was performed to decouple the acoustic and hydrodynamic contribution to pressure fluctuations within the cavity. The acoustic region contains the pressure fluctuations that propagate at the speed of sound. The acoustic wavenumbers, k_0, associated with this region are between $-\frac{f}{c}$ and $\frac{f}{c}$. The hydrodynamic region is defined by wavenumbers outside of the acoustic region. However, at low frequencies, the hydrodynamic wavenumbers are difficult to decouple from the acoustic wavenumber. Therefore, a limiting frequency is defined, below which the distinction between acoustic and hydrodynamic spectra is uncertain. This frequency is defined as[41] $f \leq U_\infty \Delta k$, where Δk is the wavenumber resolution.

The wavenumber spectra were calculated using a 2D Fourier transform applied to the pressure fluctuations sampled along the cavity centerline, as illustrated for the cylindrical cavity in Fig. 4. A Hanning window with 50% overlap was applied in the time domain using the approach described in Ref. 41. The data were sampled with a spacing of $\Delta x = 1.5 \times 10^{-2}$ cm at the top and bottom of each cavity in the streamwise direction. For the covered cavities, the pressure was sampled just below the interface between the porous region and the cavity volume. The sampling rates, number of time steps, Hanning window size (N_{fft}), and sampling locations are defined in Table III.

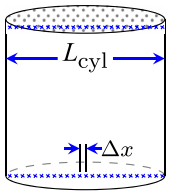

FIG. 4. Illustration of the sampling location of p' along the centerlines at the top and bottom of the cylindrical cavity, with a spacing of Δx.

3. Proper orthogonal decomposition

Proper orthogonal decomposition (POD) was used to decompose the pressure fluctuations into a linear combination of orthogonal modes to identify coherent structures.[42,43] The tool MODULO[44] was used to perform this decomposition. The pressure fluctuations were sampled from the PowerFLOW simulation output with an equal spacing of $\Delta x = \Delta z = 2.5 \times 10^{-2}$ cm. MODULO requires a Cartesian grid of equally sampled points; thus, a square grid was used. As the cavity cross-sections are circular, the data for the region outside of the cavities are padded with zeros. The sample rate and sampling location with respect to cavity depth (y) are the same as described in Table III. The resulting modes are defined in terms of their spatial structures, ϕ, and temporal bases, $\boldsymbol{\psi}$.[43] The estimated energy, i.e., the amplitude, of each mode, σ_r is weighted by $\sqrt{N_s N}$, where N_s are the number of sampled spatial points and N are the number of time samples.[43]

III. GRID AND DATA VALIDATION

A. Grid resolution validation

The effect of grid resolution on the flat plate's boundary layer profile and the pressure spectrum inside the cylindrical cavity (covered and uncovered) were evaluated using five grid refinement levels. For the uncovered simulations, these levels are specified in Table IV. The smallest voxels are located inside the uncovered cavities. The minimum size of the voxels above the flat plate, upstream of the cavity, is twice the minimum voxel size inside the cavity. Table IV lists as well the non-dimensional wall distance, y^+, from the center of the smallest voxels to the flat plate wall. The non-dimensional wall distance is defined as follows:

$$y^+ = \frac{y u_\tau}{\nu}, \tag{5}$$

where y is the vertical coordinate, u_τ is the friction velocity, and ν is the kinematic viscosity. The value of u_τ is measured $3L_{\text{Cylindrical}}$ upstream of the cavity center. Table IV shows the relative cell size between grids, h_i/h_1, where h_1 is the smallest voxel size of the finest grid tested, and h_i is the smallest voxel size of grid i. The time step in the LBM simulation is set to maintain a Courant–Friedrichs–Lewy number of 1, considering the sound speed, and is therefore dependent

TABLE III. Wavenumber-frequency spectrum calculation parameters for each cavity, normalized by $L_{cyl} = 1.0$ cm.

	Uncovered			Covered		
	Cylinder	Countersunk	Conical	Cylinder	Countersunk	Conical
Sample rate, kHz	15.32	15.32	15.32	183.8	183.8	367.6
Number of time steps	4307	4307	10 052	7353	7353	14 705
N_{fft}	512	512	512	2048	2048	2048
Δf, Hz	29.9	29.9	29.9	89.7	89.7	179.4
Δx, cm	1.5×10^{-2}	1.5×10^{-2}	1.5×10^{-2}	1.5×10^{-2}	1.5×10^{-2}	1.5×10^{-2}
Top sampling location, y/D	0.0	0.0	0.0	-1.5×10^{-2}	-1.5×10^{-2}	-2.4×10^{-2}
Top sample length, cm	1.0	1.6	4.5	1.0	1.6	4.5
Bot. sampling location, y/D	−1.0	−1.0	−1.0	−1.0	_1.0	−1.0
Bot. sampling length, cm	1.0	1.0	0.7	1.0	1.0	0.7

TABLE IV. Grids used in the convergence study (uncovered cylindrical cavity).

Grid i	Min. voxel size, m outside the cavity	Min. y^+ outside the cavity	h_i/h_1	Min. timestep, μs at VR0
Very coarse	4.00×10^{-4}	15	3	0.34
Coarse	2.67×10^{-4}	10	2	0.23
Medium	2.00×10^{-4}	8	1.5	0.17
Fine	1.60×10^{-4}	6	1.2	0.14
Very fine	1.33×10^{-4}	5	1	0.11

on voxel size. For the different grids, the time step at VR0 is shown in Table IV.

The convergence of the boundary layer velocity profile, 3.0 cm upstream of the cavities, is analyzed with respect to the displacement thickness, $\delta^\star$, and the boundary layer momentum thickness, θ. The grid dependence of $\delta^\star$ and θ is shown in Fig. 5(a). Figure 5(b) shows the convergence of the pressure fluctuations at the bottom center of the cylindrical cavity (covered and uncovered), for the one-third-octave band centered at 6.3 kHz since this band contains the acoustic depth mode for the cylindrical cavity. Furthermore, this band is associated with smaller eddies (at higher frequencies), which are therefore expected to be more sensitive to the cell size.

The fits shown in Fig. 5 are defined by

$$f(h_i) = \phi_0 + \alpha h_i^c, \tag{6}$$

where α is a constant, c is the order of convergence, ϕ_i is the parameter (e.g., $\delta^\star$) obtained from the simulation with grid i, and ϕ_0 is the estimated exact solution, i.e., the solution for a grid with infinite resolution. The order of convergence is 3.[28] ϕ_0 and α are calculated with the least squares regression described in Ref. 45. Figure 5(a) indicates that the grids with a medium, fine, and very fine resolution (see Table IV) result in approximately equal values of $\delta^\star$ and θ. Figure 5(b) also shows that the medium grid ($h_i/h_1 = 1.5$) results in a Φ_{pp}, at the bottom of the cavity, close to the estimated exact solution, i.e., the value at $h_i/h_1 = 0$ for the 6.3 kHz one-third-octave band.

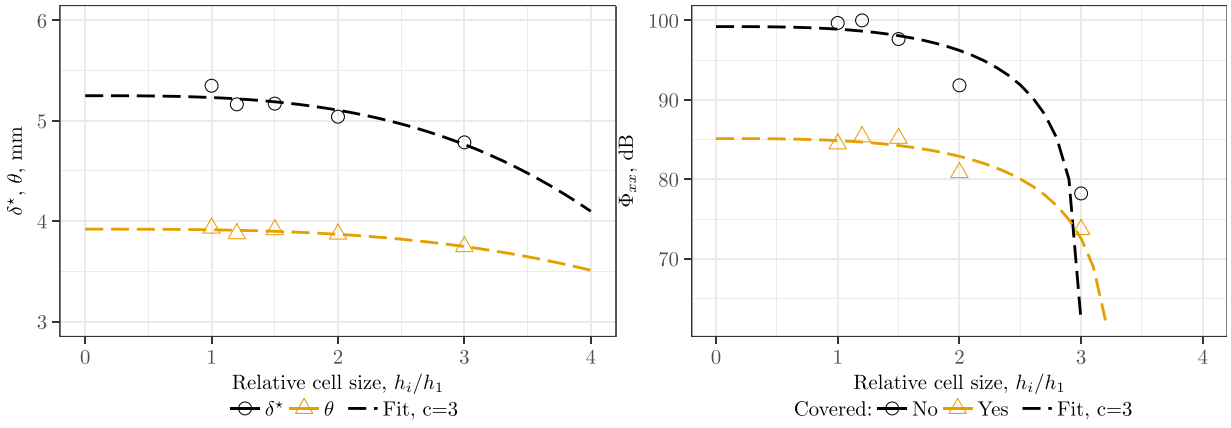

FIG. 5. Grid convergence study comparing the following variables: (a) BL displacement and momentum thicknesses, $\delta^\star$ and θ, and (b) pressure fluctuations (in the 6.3 kHz centered one-third-octave-band) at the bottom of the cylindrical cavity.

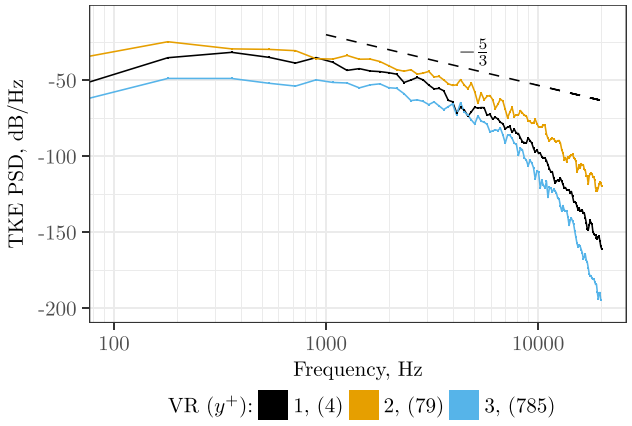

FIG. 6. PSD of the turbulent kinetic energy (TKE) at 3 VR regions over the flatplate, from the uncovered conical cavity simulation.

Based on the previous results, the fine resolution is chosen for the cylindrical and countersunk cavities (covered and uncovered). The conical cavity simulations use the medium grid resolution because it has a larger outer diameter, which increases the computational costs, particularly for the simulation with the cloth cover.

Figure 6 shows the PSD of the turbulent kinetic energy (TKE) of the simulated boundary layer at four VR regions. The TKE was calculated from the sampled turbulence (u', v', w') upstream of the conical cavity for the medium grid (Table IV). The VR1, VR2, and VR3 data were sampled at x = −3.0 cm. This figure shows that the voxel sizes for the VLES simulation are sufficiently small to simulate the turbulent eddies for this work.

Figure 7 shows the spanwise correlation of turbulent pressure fluctuations at $x = 0$ and $y = 0$, keeping as reference a point at the spanwise location of the periodic boundary. The figure shows the correlation coefficient, r, for the flatplate and uncovered cavities

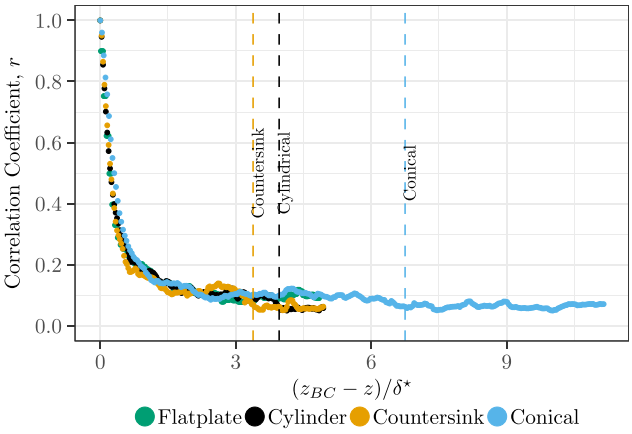

FIG. 7. Spanwise variation of correlation coefficient for the flatplate and uncovered cavities simulation. The points are sampled at the streamwise center of the domain, and at the flatplate surface height, i.e., at $x = 0$ and $y = 0$. The reference point is the spanwise location of the periodic boundary (positive z). The vertical dashed lines are the spanwise location of the cavity edges.

simulation. The correlation between pressure fluctuations at the boundary condition and at the spanwise location where each cavity begins (cavity edge) is below $r = 0.1$, being close to the minimum correlation calculated: $r_{noise} \approx 0.05$. The figure indicates that the spanwise length of the domain is sufficient for a low influence of the boundary condition in the cavity flowfield. In wall units, the distance between the periodic boundary condition and the countersunk cavity edge is $z^+ = 1.4 \times 10^3$. The spanwise distance is one order of magnitude larger than the spanwise extent of the turbulent structures characteristic of high-amplitude pressure peaks, as expected in a zero-pressure gradient turbulent boundary layer, with a similar Re_θ.[46]

B. Comparison with experiments

Figure 8 shows the experimental and simulated streamwise velocity, u, and turbulence intensity (TI) profiles of the boundary layer, measured upstream of the cavity location. The profiles from the simulation are measured 3 cm upstream of the cylindrical cavity center and the profiles for the experimentally measured profiles were sampled 10 cm upstream of the cylindrical cavity. The turbulence intensity is defined as follows:

$$\mathrm{TI} = u'/U_\infty, \tag{7}$$

where u' is the root mean square (RMS) of the streamwise velocity fluctuations in the boundary layer. The profiles are normalized with the free-stream velocity, U_∞. Figure 8(a) indicates that the simulated TBL has a slightly higher velocity deficit than the experimental TBL. The boundary layer thickness is 3.3 cm in the simulation and 3.7 cm in the experiment. This leads to a negligible difference in momentum thickness between the experiment and the simulation (below 3%). The ratio θ/L has been identified as a dominant driving parameter for cavity flow,[7,48] and the simulation and experiment have equivalent ratios. The momentum thickness-based Reynolds number is, therefore, also identical in the experiment and the simulation: $Re_\theta = 8.6 \times 10^3$. The shape factor of $\delta^*/\theta = 1.3$ is indicative of a fully developed simulated turbulent boundary layer.[49]

Figure 8(b) shows that, for $y^+ > 100$, the boundary layer TI levels in the simulation are close to those from the experiment. $y^+ \approx 50$ was the lowest wall distance at which experimental hot-wire measurements were made, due to limitations of the hot-wire measurement system. Marusic's empirical model was used to estimate the boundary layer TI profile close to the wall,[47] using experimental data as input. Marusic's empirical model estimates a boundary layer TI profile from the inputs: δ_{99}, U_∞, and u_τ. The experimental u_τ is obtained from Re_θ, using the Kármán–Schoenherr (KS) formula.[50] Figure 8(b) shows a reasonable agreement between the simulated and empirical TI profiles, with the model's estimate of TI having a lower peak. This result indicates that the highest TI levels in the simulation may be slightly higher than in the experiment. The result is associated with the (approximately 10%) higher wall shear in the simulation, in comparison with the experiment. The study focuses on the relative difference between the turbulent fluctuations upstream of the cavities and at the cavity bottoms. Therefore, small differences in turbulence levels over the flat plate, between experiment and simulation, are assumed to have minimal effect on the analysis.

Figure 9 compares the wall pressure spectra at the bottom of each cavity from the experiment with those of the simulations. ΔSPL is

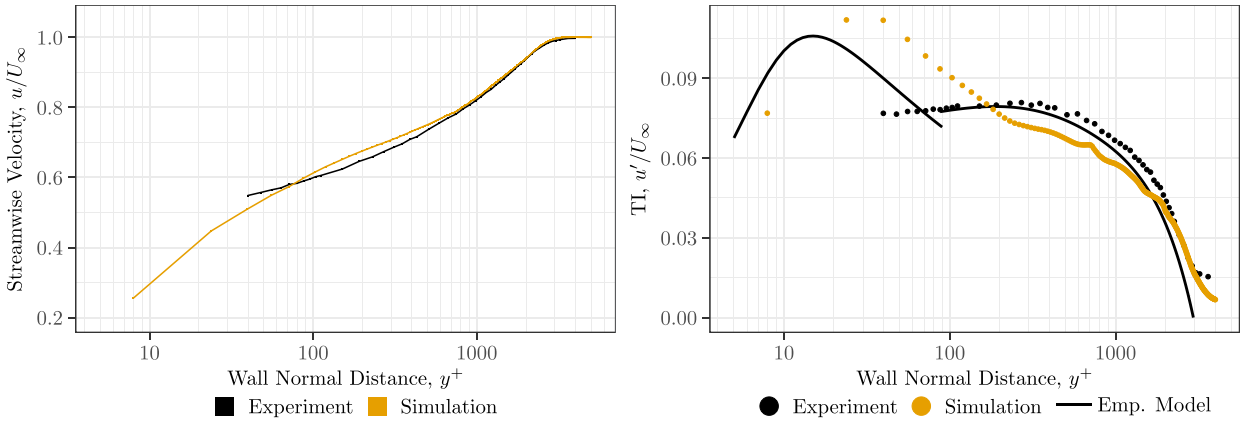

FIG. 8. Simulated and experimental boundary layer profiles: (a) velocity profile and (b) turbulence intensity profile. Empirical turbulence intensity profiles were obtained with Marusic's model.[47]

defined as the difference between the wall pressure spectrum at the bottom of the cavity and the wall pressure spectrum upstream of the cavity, i.e., the flush microphone measurement,

$$\Delta\text{SPL} = \text{SPL}_{\text{cavity}} - \text{SPL}_{\text{flush}}. \tag{8}$$

Figure 9 shows a good agreement between the numerical and experimental ΔSPL for each uncovered cavity. This indicates that the flow features that lead to pressure fluctuations at the cavity bottoms are realistically represented in the simulations. Only for frequencies above 4 kHz, do the simulations over-predict the pressure fluctuations at the bottoms. Figure 9 shows that the simulations for the covered cavities show a reduction of the TBL pressure spectra at the bottom of the cavities with respect to the flush spectrum. These trends agree with the experiment but under-predict the amount of attenuation. This result suggests that the attenuation, caused by the stainless-steel cloth cover, is higher in the experiment than in the simulation, especially toward higher frequencies. The results suggest that, when eddy size becomes small in comparison with the cavity aperture diameter (see discussion of Fig. 10), the validity of the equivalent fluid approach for simulating covered cavities is reduced. The discrepancy in the amount of attenuation is independent of the cavity geometry and is therefore considered to not affect the conclusions of this investigation.

Figure 10 shows the coherence length of the TBL pressure fluctuations calculated from a flat plate simulation without a cavity present. The sampling location of the data was centered at $x = 0$, i.e., at the cavities' streamwise location. Figure 10(a) shows that the streamwise coherence length, which is indicative of eddy size, is comparable to the cylindrical and countersunk cavity aperture diameters at low frequencies (at 1000 Hz). The spanwise coherence length of the pressure fluctuations, is considerably smaller than the cylindrical cavity's diameter, for frequencies higher than 350 Hz). As seen in previous experimental studies, e.g., Refs. 51 and 52, the coherence length agrees with Efimtsov empirical model (see dashed line) at high frequencies.

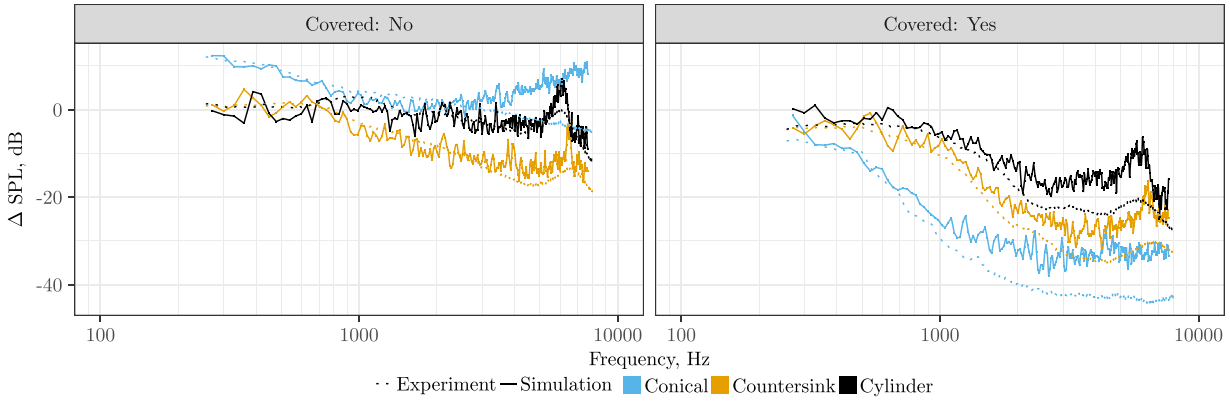

FIG. 9. Simulated and experimental pressure spectra: difference between the spectra at the bottom of the cavities, and the spectra over the flat plate for both uncovered cavities and covered cavities.

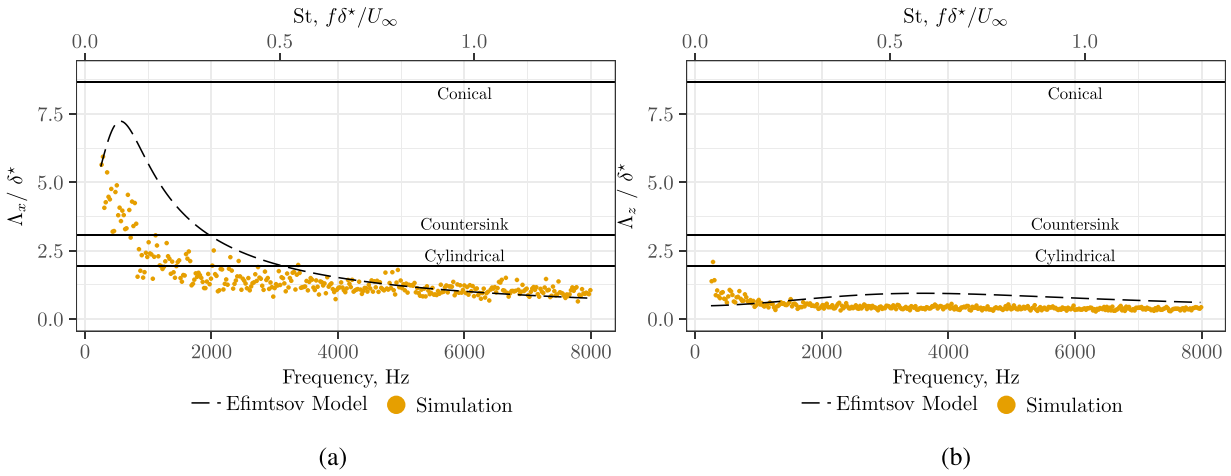

FIG. 10. Coherence length of the pressure fluctuations at $y = 0$ for the flat plate simulation, in comparison with Efimtsov empirical models: (a) streamwise coherence length and (b) spanwise coherence length. The cavity diameters are shown for reference as horizontal lines. Data extracted from a flat plate simulation (without cavity), at $x = 0$.

IV. UNCOVERED CAVITIES

A. Effect of cavity geometry on the time-averaged flowfield

Figure 11 presents the average streamwise velocity, u, and static pressure coefficient,

$$C_p = (p_s - p_\infty)/q_\infty, \tag{9}$$

inside the uncovered cavities. p_s is the static pressure, p_∞ is the free-stream static pressure, and q_∞ is the free-stream dynamic pressure. Figure 11 shows u/U_∞ and C_p in a plane aligned with the cavity center-line, $z = 0$. The streamtraces in Fig. 11 are defined as lines which follow the local in-plane velocity vector.

The comparison of Figs. 11(a) and 11(b) indicates that decreasing the wall angle ψ from 90° to 45° and increasing d_c/D to 3, for the case of the countersunk cavity, shift the center of recirculation away from

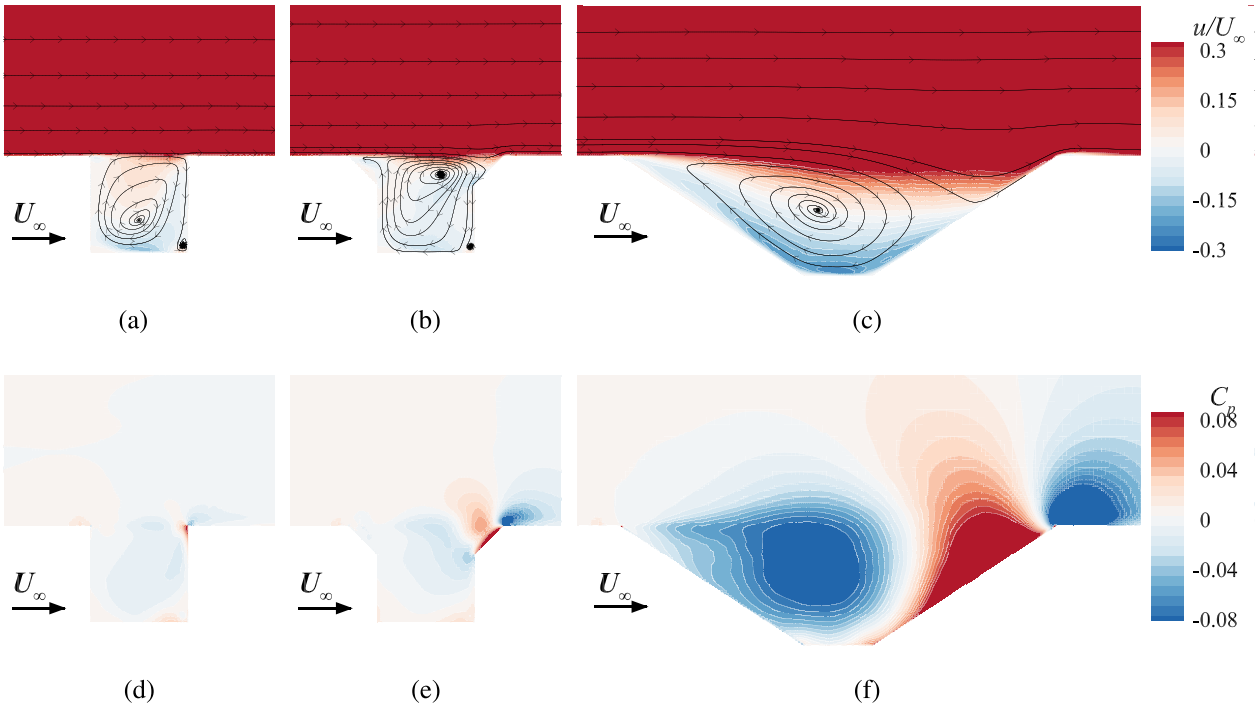

FIG. 11. Uncovered cavities average flowfield, located at the $z = 0$ plane (center of the cavities). Streamwise velocity contours and in-plane streamtraces: (a) cylindrical, (b) countersunk, and (c) conical. Pressure coefficient contours: (d) cylindrical, (e) countersunk, and (f) conical.

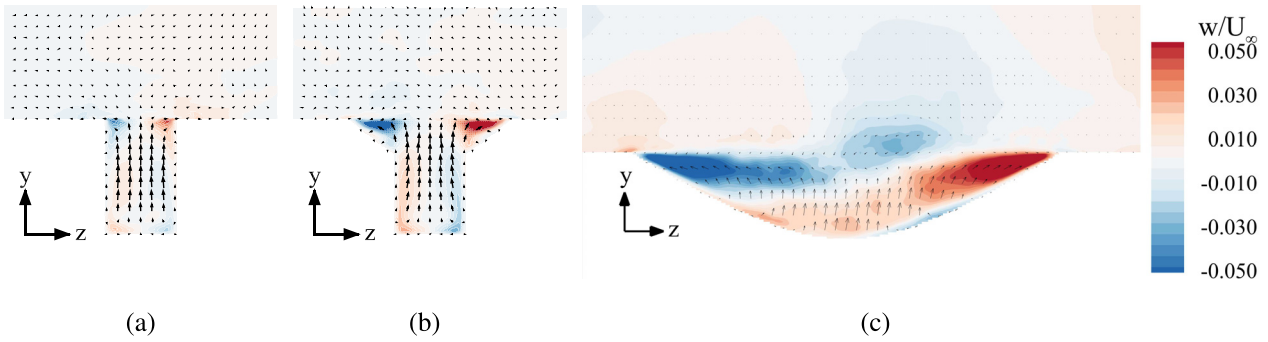

FIG. 12. Average spanwise velocity, w, contours and in-plane vectors ($x = -0.25L$ plane) for the following uncovered cavities: (a) cylindrical, (b) countersunk, and (c) conical.

the bottom, resulting in a lower velocity along the bottom when compared to the cylindrical cavity. Figure 11(c) indicates that further increasing d_c/D to 1.0 (see Fig. 1) and increasing the cavity aperture, increases the recirculation velocities at the bottom, in contrast with the countersunk cavity. Furthermore, the streamtraces in Fig. 11(c) indicate that, due to the upstream wall angle, the stagnation point on the downstream cavity wall moves toward the bottom, changing the recirculation pattern. Shifting the recirculation toward the bottom of the cavity increases pressure fluctuations at the bottom, as it leads to the convection of eddies from the boundary layer toward the bottom. Additionally, higher velocities inside the cavity are associated with higher shear forces, which generate turbulence. The wall friction due to increasing cavity wetted area has a minimal effect on recirculation because the reduction in velocity at the bottom does not increase substantially with the increasing wetted area.

A comparison of Figs. 11(d) and 11(e) shows that the downstream angled wall of the countersunk cavity leads to regions of higher positive and negative C_p, with a corresponding larger pressure gradient. The downstream edge of the conical cavity also leads to a high C_p region at the stagnation point inside the cavity [Figs. 11(c) and 11(f)]. Pressure gradients can accelerate or decelerate the flow inside the cavity, further increasing the shear forces acting on the fluid.

Figure 12 shows average spanwise velocity, w, contours in the $x = -0.25L$ plane. The angled walls of the countersink and conical cavities increase the spanwise velocity at the top, compared to the cylinder, as shown in Figs. 12(b) and 12(c). This result and the previous one indicate that the upstream angled wall of the countersunk and conical cavities cause stronger velocity fields within the cavities that contribute toward increased pressure fluctuations, i.e., turbulence, at the top of the cavity.

B. Influence of wall angle and countersink depth on pressure fluctuations

Figure 13 shows the contours of the root mean square of the pressure fluctuations, p'_{rms}, for the uncovered cavities. This figure shows that p'_{rms} is higher in the shear layer at the top of the cavities due to the local turbulence generation and vortex shedding. Beneath the shear layer, the differences between the cavities are associated with the cavities' respective recirculation patterns, as discussed previously. p'_{rms} increases near the downstream walls and the bottoms of the cavities compared to the upstream wall where the local velocity is lower. Decreasing the recirculation velocity at the bottom results in lower values of p'_{rms} as seen when comparing the countersunk cavity in Fig. 13(b) to the cylindrical [Fig. 13(a)] and conical cavities [Fig. 13(c)].

Decreasing the downstream wall angle from 90° [Fig. 13(a)] to 45° [Fig. 13(b)] or from 45° to 30° [Fig. 13(c)] increases the levels of p'_{rms} in the vicinity of the stagnation point. This location is where vortex impingement and subsequent deformation occurs, due to strong pressure gradients in the region. However, the effect of decreasing downstream wall angle on p'_{rms} at the bottom is minimized when the cavity has a countersink depth ratio of 0.3, as indicated by the

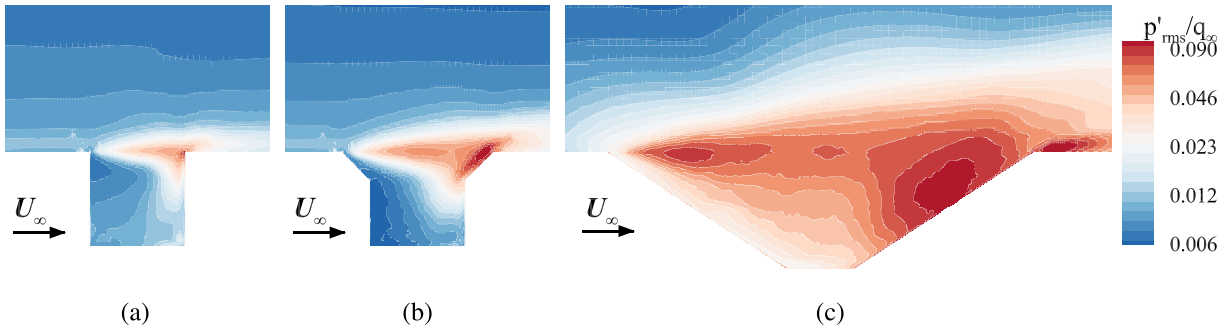

FIG. 13. Contours of the root mean square of the pressure fluctuations, for the uncovered cavities: (a) cylindrical, (b) countersunk, and (c) conical.

comparison between cylindrical and countersunk cavities [Figs. 13(a) and 13(b)]. Decreasing the upstream wall angle from 90° to 30° increases p'_{rms} within the shear layer. This is in line with the inclined angle backward facing step flow results presented in Ref. 14.

Figure 14 shows the pressure contours and the vortices present in an instantaneous streamwise slice at $z = 0$. The λ_2 criterion is used to identify vortices, where $\lambda_2 < 0$ indicates vortex structures.[53] The streamtraces show instantaneous convection paths for vortices within the cavities.

The shedding location of the Kelvin–Helmholtz type vortices[6] is near the spanwise center ($z = 0$) of the upstream edge of the cylinder in Fig. 14(a). For the cylindrical cavity, these vortices are of approximately constant size in the spanwise direction. The vortices are convected within the shear layer until they impinge on the downstream wall, emitting a pressure wave, or are convected toward the cavity bottom. Decreasing the wall angle alters the convection path of the vortices and results in the vortex shedding behavior becoming increasingly unsteady. This is shown in Figs. 14(b) and 14(c). When ψ decreases to 45°, for the countersunk cavity, the vortices exhibit similar shedding behavior as the cylindrical cavity. However, the recirculation region at the angled downstream wall entraps and distorts the shed vortices, which partially explains the larger region of elevated turbulence spread along the angled downstream wall shown in Fig. 13(b). This is in contrast to the cylindrical cavity where the region of elevated turbulence is concentrated in the shear layer. However, unlike the cylindrical cavity with $d_c/D = 0$, the vortices for the $d_c/D = 0.3$ case tend to be transported away from the cavity bottom, reducing p'_{rms} at the cavity bottom. For the conical cavity, the large region of pressure fluctuations shown in Fig. 13(c) is explained by the vortices not following a well-defined streamtrace and thus impinging at random locations along the downstream wall as well as the flowfield induced by the conical cavity's upstream angled wall increasing the deformation of the vortices.

The regions of negative C_p, shown in blue in Figs. 14(a) and 14(b) for the cylindrical and countersunk cavities, correspond to the vortex cores,[6] an example of which is indicated with an arrow in Fig. 14(a). When these vortices impinge on the downstream wall, a rarefaction acoustic wave is produced and propagates from the impingement location.[6] The resulting negative pressure from this wave can be seen within the cylindrical cavity in Fig. 14(a). Acoustic compression waves

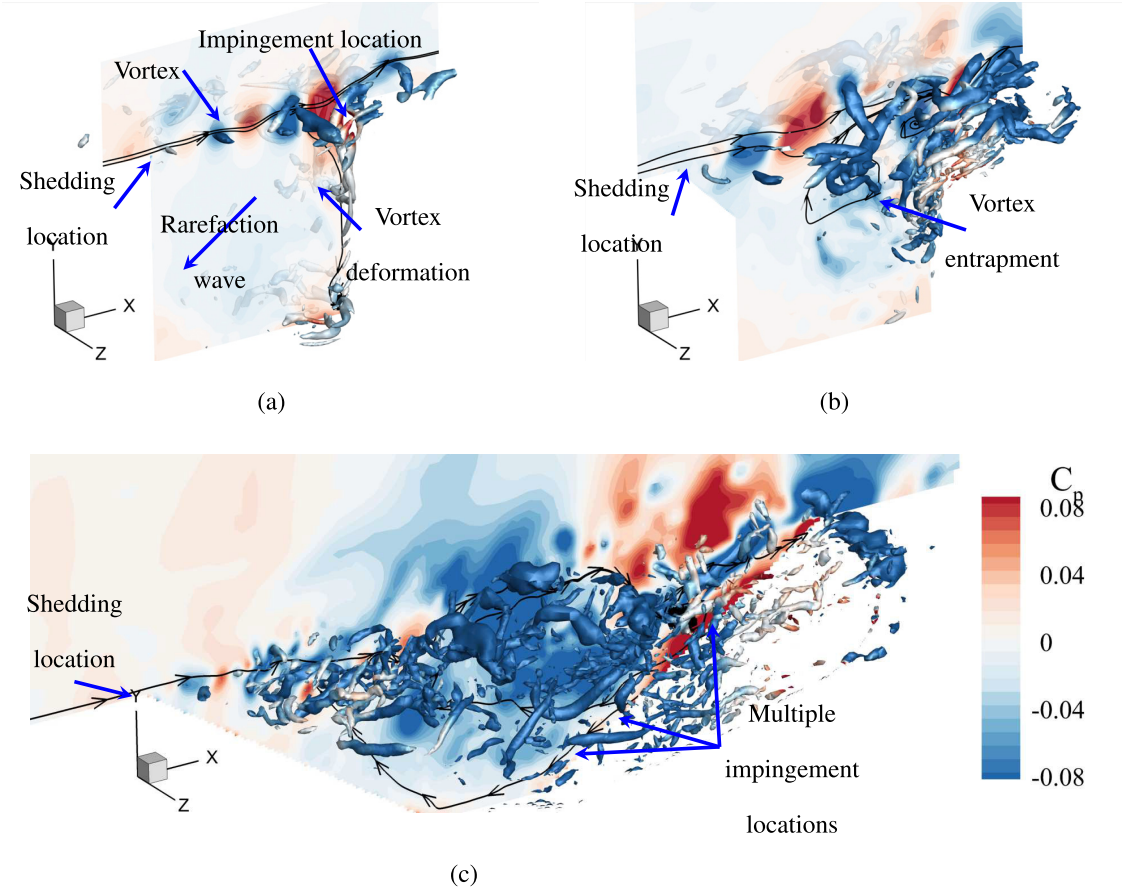

FIG. 14. Instantaneous visualization of the pressure fluctuation contours, p', vortex shedding, and velocity streamtraces. Vortex cores are identified using the λ_2 criterion with the isosurfaces defined by $\lambda_2 < -2 \times 10^8$ for the following cavities: (a) cylindrical, (b) countersunk, and (c) conical.

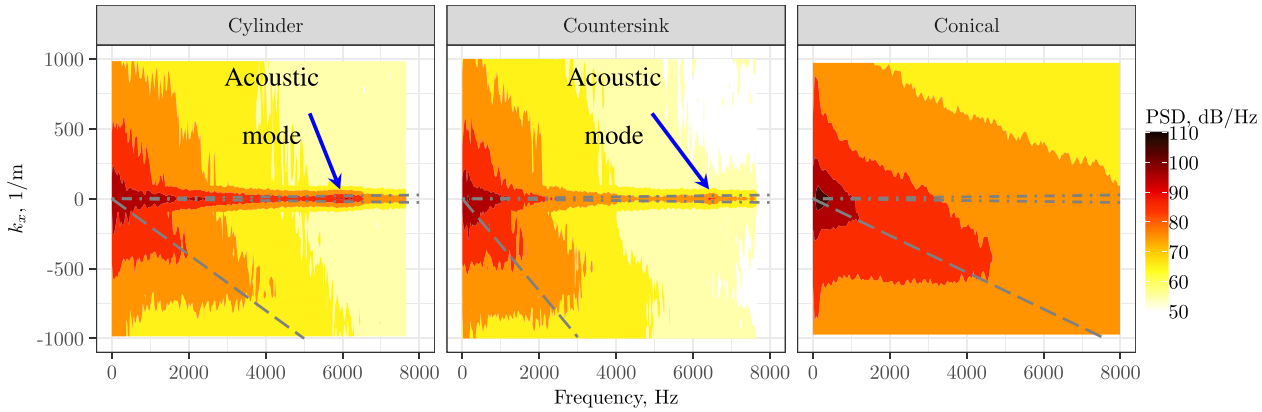

FIG. 15. Wavenumber-frequency spectra across the bottom of the uncovered cavities (dashed lines) lines represent the hydrodynamic peak due to recirculation, (dashed dotted lines) represents the area between the acoustic region. $p_{ref} = 2.0 \times 10^{-5}$ Pa.

are generated in between the impingement of these vortices, as described by Ref. 5. Unlike the cylindrical and countersunk cavities, the pressure fluctuations within the conical cavity are not substantially influenced by vortex impingement.

1. Hydrodynamic and acoustic components of the pressure spectra

The wavenumber-frequency spectra at the bottom of the uncovered cavities are shown in Fig. 15. In this figure, the contributions to the spectrum by both the hydrodynamic and acoustic phenomena are seen. The spectra within the hydrodynamic regions are concentrated near the wavenumbers, $k = \frac{f}{U_c}$, associated with the recirculation velocity, i.e., U_c along the bottom of the cavity. This velocity is -4.9, -3.0, and $-7.6\,\mathrm{m\,s^{-1}}$ for the cylindrical, countersunk, and conical cavities. The spectrum levels within the hydrodynamic region decrease with decreasing recirculation velocity due to the reduced transport of turbulence across the bottom. The spectra in and near the acoustic regions, seen for the cylindrical and countersunk cavities, are due to the pressure waves from the vortices impinging on the downstream wall. Peaks at 6.0 and 6.3 kHz are the cylindrical and countersunk cavity acoustic depth modes. However, the conical cavity does not have a well-defined acoustic region. This suggests that the scattered energy due to the vortex impingement seen in Fig. 14(c) does not result in strong pressure waves from the downstream wall. At the top of all cavities (not shown), the spectrum levels are highest near the TBL convective wavenumber, k_c, which is defined as $k_c = \frac{f}{U_c}$. The flow at the top of the cavities has a convective velocity, $U_c = 18\,\mathrm{m\,s^{-1}}$, which is 52% of the free stream velocity, U_∞.

Figure 16 shows the pressure spectra for the acoustic and hydrodynamic components of the pressure field. The acoustic component is calculated by integrating the spectrum within the acoustic wavenumber domain, while the hydrodynamic component is represented by the integrated spectrum outside this acoustic region. In these simulations, the cavity diameters are smaller than the acoustic wavelength, i.e., for frequencies below 34 kHz for the cylindrical cavity. Therefore, the

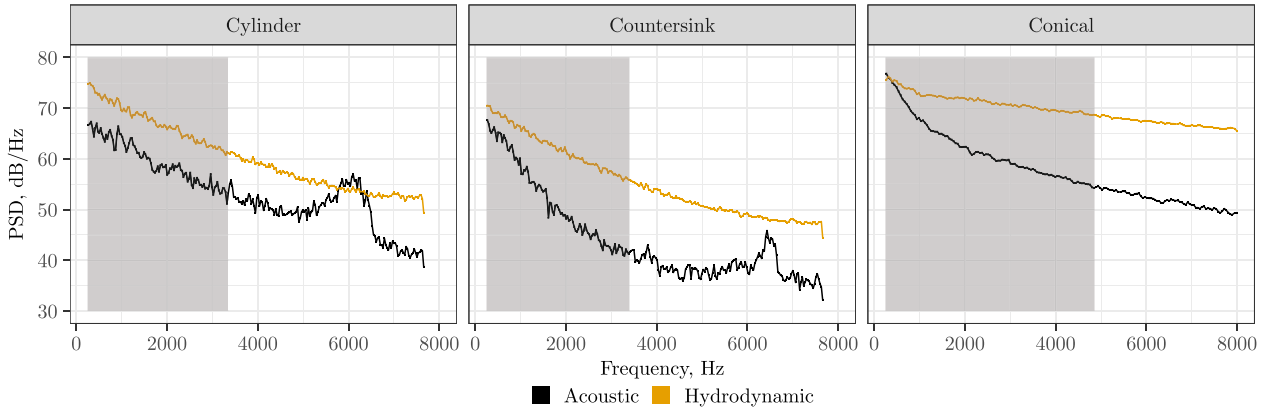

FIG. 16. Wavenumber spectra decomposed into acoustic and hydrodynamic components for all three uncovered cavities. Shaded area is the region of uncertainty, defined as $f \leq U_\infty \Delta k$.

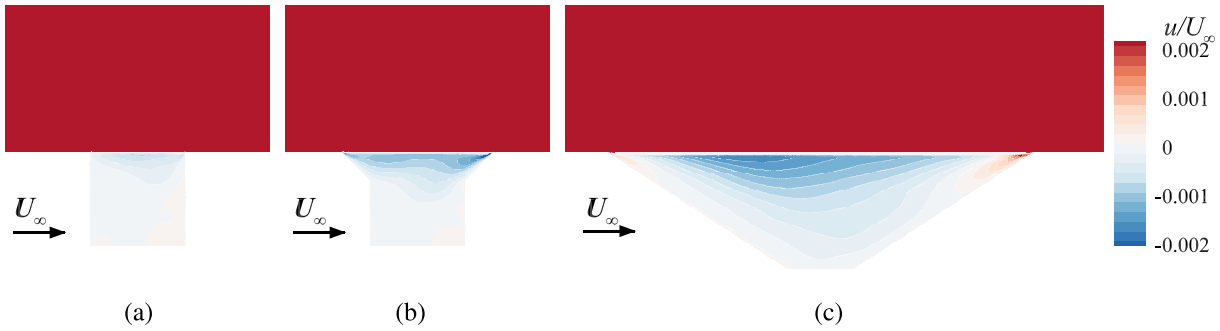

FIG. 17. Average streamwise velocity field for the following covered cavities: (a) cylindrical, (b) countersunk, and (c) conical.

wavenumber resolution, Δk_x, is larger than the acoustic wavenumber, $k_0 = f/c_0$, below this frequency. $\Delta k_x = 1/L$ is 100 m^{-1} for the cylinder and countersunk cavities, and is 142 m^{-1} for the conical cavity. As a result, the spectral energy of the acoustic region is concentrated in the $k_x = 0$ region. The shaded area in the figures highlights the frequency bands where differentiating between acoustic and hydrodynamic is difficult.

The hydrodynamic components of the spectra in Fig. 16 are dominant relative to the acoustic component for all three cavities. The cylindrical cavity's acoustic depth mode at 6.0 kHz is identifiable in the spectrum of the acoustic component and has an amplification of 8.5 dB with respect to the broadband spectrum level. The frequency of this depth mode agrees with predictions, using the expression $f = \frac{(2n+1)c_0}{4D+\delta}$, where n is the mode number beginning at 0, c_0 is the speed of sound, and δ is the correction term for the cavity diameter.[54] The acoustic component is higher for the cylindrical cavity than those of the other cavities due to the stronger pressure waves generated by the impinging vortices. The countersunk cavity's hydrodynamic component is lower than that of the cylindrical cavity due to the lower recirculation velocity. The countersunk cavity's depth mode at 6.3 kHz is also identifiable within the acoustic component of the spectrum. The countersunk cavity's acoustic mode is amplified by 7.5 dB, which is less than the cylindrical case due to the higher countersunk ratio of 0.3 resulting in a shallower straight walled portion.[54] The conical cavity's hydrodynamic component is higher than its acoustic component because the vortex impingement produces lower amplitude pressure waves compared to the other cavities. Additionally, the flow along the downstream wall transports turbulence across the bottom resulting in higher pressure fluctuations. This explains the higher hydrodynamic spectral levels for the conical cavity compared to the other two cavities. The depth mode for a conical cavity is estimated to be at $f = 5.0$ kHz using the method described in Scavone.[55] This mode is not identifiable, presumably because conical cavities have much weaker depth modes than straight walled cavities due to their lower quality factor.[54]

V. COVERED CAVITIES

In contrast to the uncovered cavities, the streamwise velocity magnitudes of the covered cylindrical, countersunk, and conical cavities are below $0.002U_\infty$, as shown in Fig. 17. Therefore, the flow beneath the cover is nearly stagnant. Covering the cavities eliminates the dominant propagation mechanism of the pressure fluctuations. As expected, eliminating recirculation partially explains why the covered cavity spectra in Fig. 9 are lower than the uncovered cavities.

A. Pressure fluctuations due to TBL eddies over the covering

Figure 18 shows the band-pass filtered pressure at the 1 kHz one-third-octave band for each cavity. This frequency band was chosen because the integral length scale of the eddies, as shown in Fig. 10(a), is of the order of the diameter of the cylindrical cavity. The TBL eddies

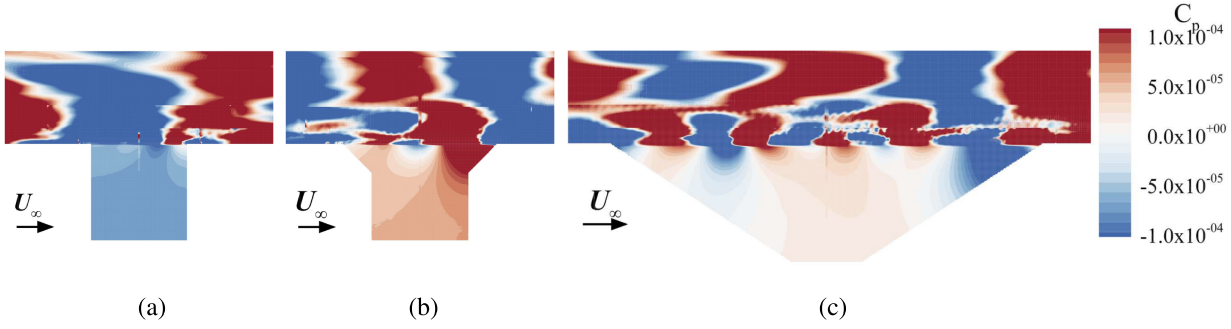

FIG. 18. Band-pass filtered pressure fluctuations at the 1.0 kHz one-third-octave frequency band. The streamwise slice is centered at z = 0.0 cm for the following covered cavities: (a) cylindrical, (b) countersunk, and (c) conical.

convect across the top of the covering at the boundary layer convective velocity, U_c.[56] Immediately above the covering, $y = 0.0$ cm, the pressure fluctuations due to the eddies are visible. The distance between these eddies is indicative of the TBL streamwise coherence length, which approximates the size of the eddies. The eddies immediately above the cover create a pressure field inside the cavity. This pressure field decays as it expands within the cavity volume. This pressure field is the dominant source of noise (p') at the bottom of the covered cavities and can be considered a near field acoustic perturbation.

The cylindrical cavity band-passed pressure field is shown in Fig. 18(a). The pressure field within the cavity is almost spatially uniform (coherent) due to the eddies at the top of the cavity being close in size to the cavity aperture size. As a result, the pressure field within the cavity is highly coherent with respect to the microphone location (center of the cavity bottom). The countersunk cavity in Fig. 18(b) exhibits similar behavior as the cylindrical cavity with the pressure field becoming increasingly uniform toward the cavity bottom. At the top, the eddies are smaller than the aperture size. This results in a more complex pressure field at the top of the cavity, especially near the angled walls. The pressure field within the conical cavity, shown in Fig. 18(c), is much less uniform than the other cavities. This is due to the aperture being approximately a factor of 4.5 larger than the eddies, as indicated by Fig. 10(a). The resulting pressure field within the conical cavity is the summation of the rarefactions and compressions at the top. The eddies immediately above the conical cavity center contribute to p' at the microphone location. This is shown by Fig. 18(c).

1. Hydrodynamic and acoustic components of the pressure fluctuations

The wavenumber-frequency spectra for the cylindrical cavity are shown in Fig. 19. Figure 19(a) shows the spectrum just beneath the covering, $y = -1.5 \times 10^{-3}$ cm. The covering reduces the amplitude of the spectrum at the top of the cavities compared to the uncovered case in Fig. 15 by approximately 20 dB. The spectral energy is more concentrated near the convective wavenumber, k_c, as shown by a similar wavenumber analysis in Ref. 57. This convective ridge is due to the convecting eddies within the TBL being the primary source of pressure fluctuations. At the bottom of the cylindrical cavity, shown in Fig. 19(b), the spectrum is highest at or near the acoustic wavenumber, k_0, i.e., at the bottom of the cavity the pressure fluctuations propagate primarily at the speed of sound. The countersunk and conical cavities exhibit similar wavenumber-frequency spectra.

Figure 20 compares the hydrodynamic and acoustic components of the spectra at the bottom of all three covered cavities. The acoustic component is dominant at the bottom of all covered cavities. For the covered cylindrical cavity, the acoustic contribution is approximately 20 dB higher than the hydrodynamic contribution at the bottom. The depth mode is visible near 6.0 kHz with a reduced amplitude compared to the uncovered cavity in Fig. 16. The porous cover changes the acoustic impedance at the top of the cavity and consequently reduces the quality factor of the cavity.[54] The countersunk cavity's spectrum levels are 5–10 dB lower than the cylindrical cavity. The depth mode is also visible at 6.3 kHz. The covered conical cavity reduces the acoustic spectrum by an additional 10 dB for frequencies greater than 4.0 kHz compared to the countersunk cavity. A small peak near the conical cavity's predicted depth mode can be seen near 4.5 kHz. The acoustic component of the TBL spectra levels at the bottom decrease with increasing cavity aperture size.

2. Modal decomposition of p′

Proper orthogonal decomposition was performed on the pressure fluctuations in the 2D plane at the top (under the covering) and bottom of the covered cavities. Figure 21 shows the first three mode shapes, ϕ_r, sorted by the energy content of each mode, σ_r, at the top of a covered cylindrical cavity. The energy of each mode, as a percentage of the sum of the energy of all the modes, is illustrated by the vertical gray bar. The first mode contains about 61% of the total energy and resembles an acoustic plane wave mode ($m = 0$, $\mu = 1$), where m is the azimuthal mode number, and μ is the radial mode number.[58] This work uses the numbering convention where the radial mode number index begins at 1, per the Refs. 59 and 58. This mode is dominant because the cavity diameter is close to the eddy size for frequencies below 2.0 kHz, shown in Fig. 10. Modes 2 and 3 have the same shape

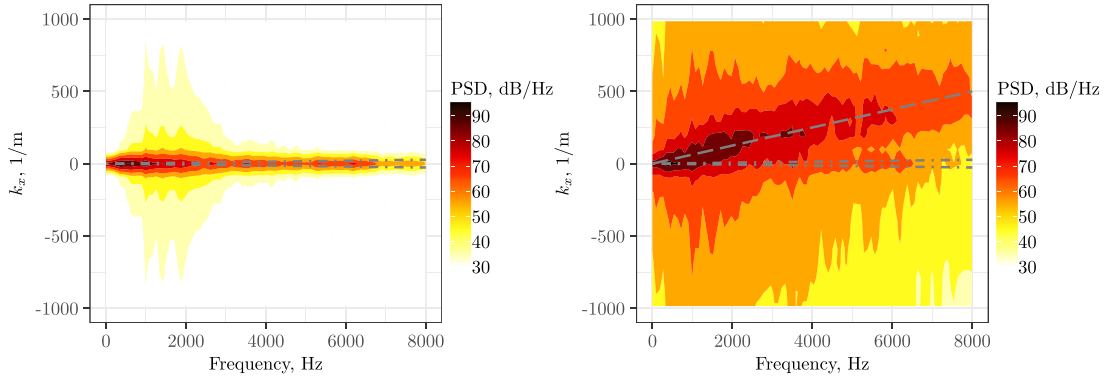

FIG. 19. Wavenumber-frequency spectra across the covered cylindrical cavity (dashed lines) lines represent the hydrodynamic peak, (dashed dotted lines) represents the area between the acoustic region. $p_{ref} = 2.0 \times 10^{-5}$ Pa. (a) Top of the cylindrical cavity; (b) bottom of the cylindrical cavity.

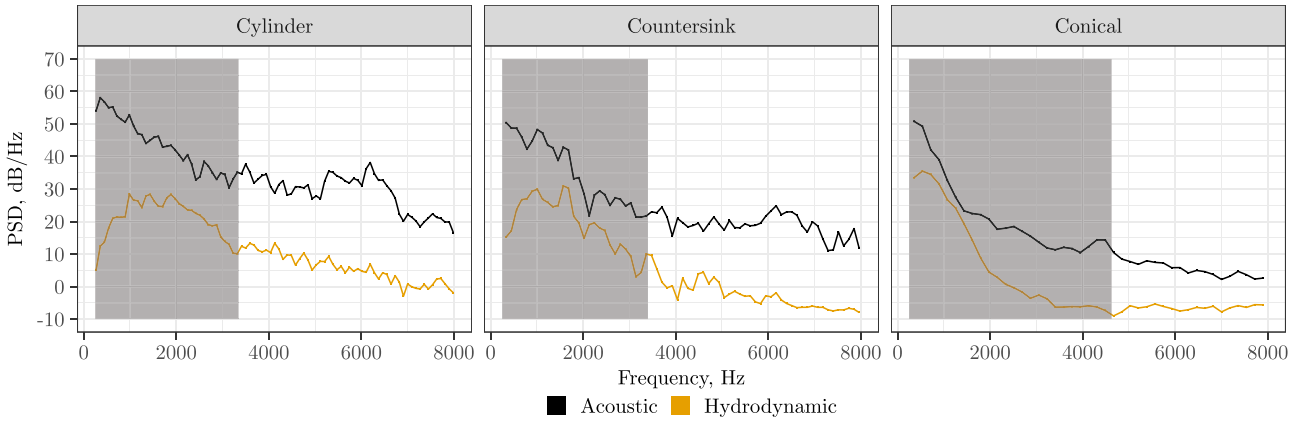

FIG. 20. Decomposition of the wavenumber spectra into acoustic and hydrodynamic components for all three covered cavities. Shaded area is the region of uncertainty.

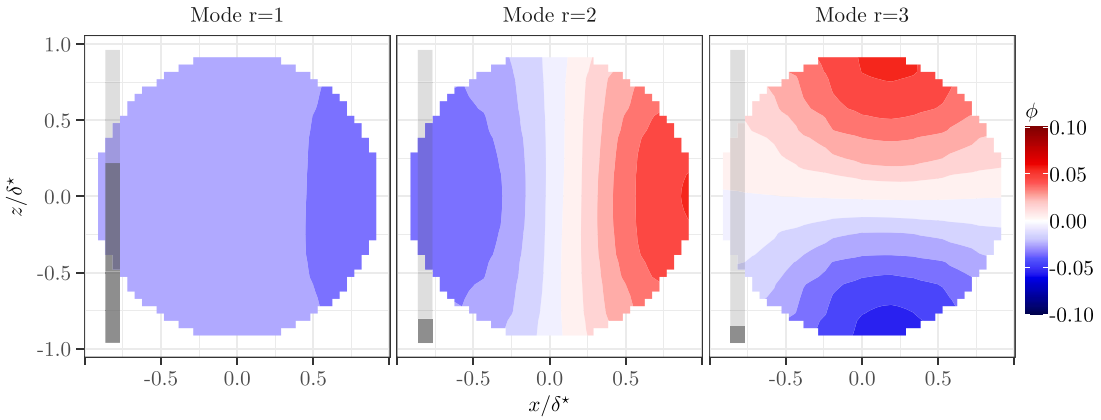

FIG. 21. First three mode shapes, ϕ, at the top of the covered cylindrical cavity, y $= -1.5 \times 10^{-2}$ cm. The modes are sorted by energy content, with the gray bars indicating the percentage of total energy, $\sum \boldsymbol{\sigma}$, each mode contains.

as the acoustic modes in a circular duct.[58] Specifically, they are the $m=1$, $\mu = 1$ acoustic mode. Thus, Fig. 21 suggests that acoustic modes are dominant when the eddy size is larger than the cavity aperture.

The first three POD modes at the top of the covered conical cavity are shown in Fig. 22. Unlike the cylindrical cavity, whose first mode represents the majority of the energy in the pressure field, the energy at the top of the conical cavity is spread out across more modes, with the first mode having only 1.3% of the total energy. This is due to the conical aperture diameter being larger than the TBL streamwise coherence length, as shown in Fig. 10. The mode shapes do not correspond to acoustic mode shapes as the pressure fluctuations are not coherent with a single eddy due to the conical cavity diameter being a factor of 4.5 larger than the cylindrical diameter.

At the bottom of the covered cavities, the mode shapes correspond to the acoustic mode shapes of a circular duct. This is shown in Fig. 23 for the conical cavity. POD mode 1 is similar to the acoustic plane wave mode, $(m=0, \mu = 1)$, mode 2 corresponds to the acoustic mode $(m=1, \mu = 1)$, mode 4 is similar to the acoustic mode $(m=2, \mu = 1)$, mode 6 matches the $(m=0, \mu = 2)$ mode, mode 8 is the $(m=3, \mu = 1)$ acoustic mode, and mode 10 is the $(m=1, \mu = 2)$ mode. The first POD mode contains the largest percentage of the total estimated energy, 83%. This is in contrast to the same mode at the top in Fig. 22. The explanation is that the higher order modes are cut off in the cavity and thus exponentially decay as they propagate toward the bottom of the cavity.[58,60] The first mode and its associated energy propagate to the cavity bottom resulting in it containing the majority of the energy at the cavity bottom. The cutoff condition is defined by the following expression:

$$\frac{\omega a}{c_0} > \alpha_{m\mu}, \tag{10}$$

where a is the cavity aperture radius and $\alpha_{m\mu}$ is the radial wave number. The radial wavenumber is the Bessel (of the first kind) derivative root.[58] For example, for mode $n=2$ in Fig. 23 $(m=1, \mu = 1)$ the root of the Bessel function of the first kind derivative is $\alpha_{11} = 1.8412$.

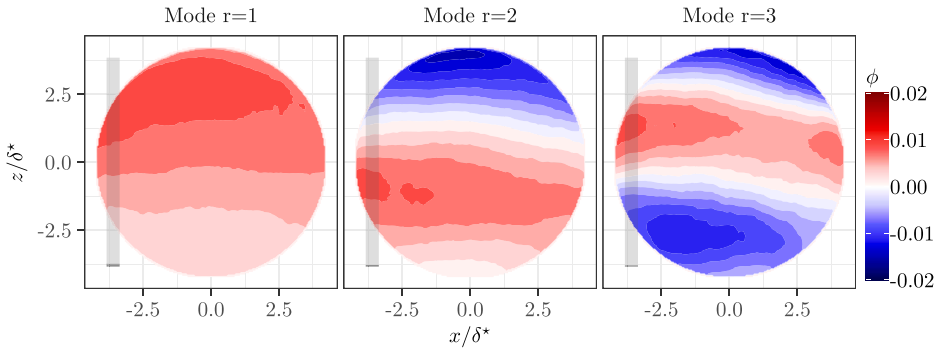

FIG. 22. First three mode shapes, ϕ, at the top of the covered conical cavity, y $= -1.5 \times 10^{-2}$ cm. The gray bars indicate the percentage of total energy, $\sum \boldsymbol{\sigma}$, each mode contains.

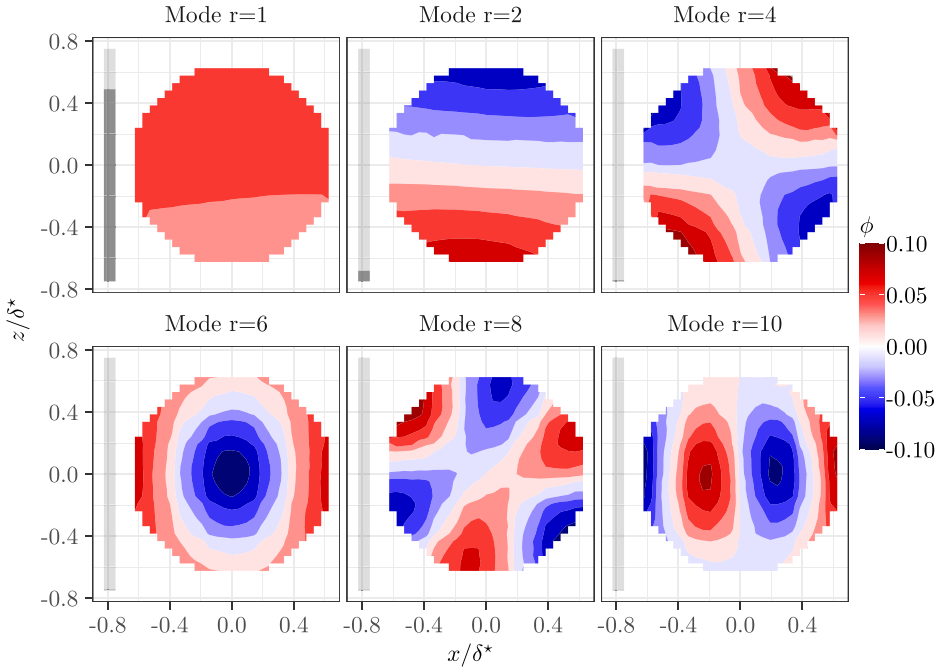

FIG. 23. First six unique modes, ϕ, at the bottom of the covered conical cavity. The gray bars indicate the percentage of total energy, $\sum \boldsymbol{\sigma}$, each mode contains.

Equation (10) states that for the cylindrical cavity with a diameter of 1.0 cm the first non-planar acoustic mode will propagate for frequencies above 20.1 kHz. Therefore, only mode 1, the planar mode, is cut on for the frequencies of interest and propagates without decaying.

The effect of cavity aperture size on the attenuation of the TBL spectra is shown in Fig. 24. This figure shows the normalized energy content of each mode, $\sigma_r/||\boldsymbol{\sigma}||$, where $||\boldsymbol{\sigma}|| = \sqrt{\sigma_1^2 + \sigma_2^2 + \cdots + \sigma_r^2}$, at the cavity top and bottom for all three covered cavities. At the top of the cylindrical cavity, the normalized amplitude of the first mode is 18 dB higher than the next highest mode. As the cavity aperture diameter increases for the countersunk and conical cavities, the difference between the first two modes at the cavity tops decreases to 10 and 5 dB. Thus, the energy of the TBL pressure field is increasingly spread across the higher order POD modes for larger cavities. This is due to the cavity aperture size increasing with respect to the coherence length of the TBL and therefore the number of pressure rarefactions and compressions present at the top of the larger cavities, due to the TBL eddies, increases. In contrast, the pressure fluctuations at the top of the smaller cavities can be represented primarily by the planar mode as it contains significantly more energy because the TBL eddies convecting over the cavity are larger than the cavity, as shown in Fig. 10(a).

At the bottom of all cavities, the first mode has a 30–40 dB higher amplitude that the next highest mode. This is explained by this mode being planar and thus cut on. The higher-order modes are cutoff, thus their energy decays exponentially as they propagate from the top to the cavity bottom. Furthermore, as the cavity aperture size increases, the energy at the bottom of the cavity is increasingly concentrated in the first mode, as shown by the conical cavity having a normalized amplitude 6 dB higher than the cylindrical cavity. This is attributed to the TBL energy being spread out over higher-order modes. Therefore, larger diameter covered cavities will attenuate the TBL pressure fluctuations more than smaller ones. This explains why the covered conical cavity attenuates the TBL pressure fluctuations the most, as plotted in Fig. 9.

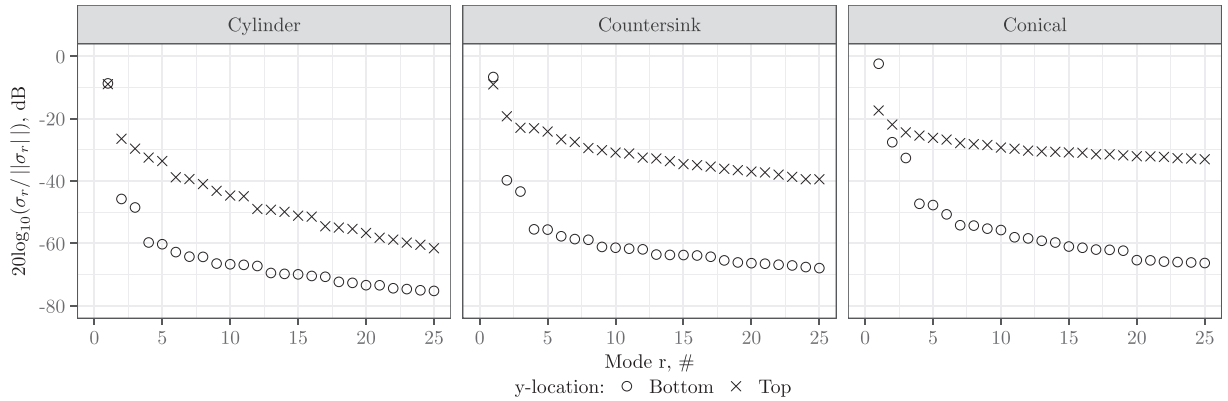

FIG. 24. Normalized energy per mode, $\sigma_r/||\boldsymbol{\sigma}||$, at the top and bottom of the cavities with a stainless-steel cloth covering.

An important result of the wavenumber and POD analyses is that the pressure field beneath a covered cavity exhibits behavior similar to an acoustic wave propagating in a duct. The wavenumber analysis in Fig. 20 shows that at the bottom of the cavity the pressure spectral energy is primarily contained within the acoustic wavenumber domain. The POD analysis shows that the pressure fluctuations at the bottom are decomposed into mode shapes that correspond to acoustic circular duct modes. This suggests that modeling the propagation of the TBL pressure field into a covered cavity can be simplified with an acoustic model, thus decoupling the acoustic from the hydrodynamic contributions to the pressure spectra at the bottom of the cavities.

VI. CONCLUSIONS

The present study used the lattice Boltzmann-based commercial software package PowerFLOW to simulate turbulent flow with a freestream velocity of 32 m s^{-1} over axisymmetric cavities placed in a flat plate. The following geometries were simulated: a cylindrical cavity, a countersunk cavity, and a conical cavity. In addition to simulating these open cavities, the effect of a finely woven stainless steel cloth covering is evaluated by using an equivalent fluid approach, modeled by imposing Darcy's law, at the top of each cavity. The simulated pressure spectrum at the bottom of the cavities is validated with experimental measurements. Both show that the uncovered countersunk cavity has the lowest TBL spectrum, followed by the uncovered cylindrical and uncovered conical cavities. The simulated trend in covered cavity performance is also in agreement with the measurements. The covered conical cavity attenuates the pressure fluctuations at the microphone location (cavity bottom) the most and therefore performs the best. The covered countersunk cavity performs better than the covered cylindrical cavity. The porous medium model is found to be capable of modeling the effect of covering the cavities. This analysis identifies the behavior of the hydrodynamic and acoustic components of the pressure fluctuations within these axisymmetric cavities.

Based on a wavenumber analysis, it is found that the pressure fluctuations at the bottom of uncovered cavities are dominated by hydrodynamic phenomena. These phenomena include recirculation and turbulence generation inside the cavities. Adding a countersink at the top of the cylindrical cavity is found to reduce recirculation toward the cavity bottom by shifting the center of recirculation away from the cavity bottom. However, extending the countersink to the bottom (conical cavity) increases the recirculation velocity and turbulence generation at the bottom. It is reasoned that the upstream angled wall deflects the flow downward and thus moves the downstream shear layer reattachment point toward the bottom, increasing the recirculation velocity. This is most noticeable in the conical cavity. Furthermore, the angled downstream walls also cause strong pressure gradients inside the cavities, which are associated with turbulence generation in the region of vortex impingement. Based on these observations, an optimal uncovered cavity should feature a perpendicular upstream wall to reduce turbulence generation and inflow, an angled downstream wall to reduce the effect of vortex impingement, and a countersink that does not extend to the bottom of the cavity to reduce the recirculation at the bottom.

Covering the cavity opening with the cloth reduces the flow across the covering, mitigating the entrance of turbulent structures into the cavity. The flow is mostly stagnant inside the covered cavities, and turbulent structures are not produced inside. The pressure field within the cavities is due to the pressure fluctuations generated by the eddies convecting across the top. The pressure field created by the TBL eddies propagates toward the bottom of the cavities at the speed of sound, as shown by the wavenumber analysis. The pressure field within the cavities is dependent on the cavity size relative to the eddy size. When the cavity diameter is nearly the same size as the eddy, the pressure field within the cavity is coherent with the pressure fluctuations corresponding to the convecting eddy. When the cavity is larger than the eddies, the pressure field from individual eddies is evanescent resulting in attenuation of the pressure field at the cavity bottom.

The proper orthogonal decomposition (POD) analysis shows that the energy distribution of the resulting orthogonal modes at the top of each cavity is dependent on cavity aperture size. For smaller apertures, the energy is concentrated in the first mode due to the cavity size being close to that of the eddy size. For larger cavities, e.g., the conical cavity, a larger ratio of the energy is decomposed into higher order

modes with less energy, relative to the smaller cavities, in the first mode. The spectra at the bottom of the cavities is attributed to the first POD mode as this mode is cut on. By shifting more energy into cutoff modes, the larger cavities have lower spectra levels at the cavity bottom. At the bottom of all cavities, the POD modes correspond to acoustic duct mode shapes. This is an important finding as it suggests that the propagation of TBL pressure fluctuations for covered cavities can be accurately modeled with an acoustic approach. The acoustic modeling could be performed using the same approach as Ref. 54. With this approach, a pressure field representative of the TBL at the top of the cavity could be simulated as propagating acoustically into the cavity.

Covered cavities reduce the TBL spectral levels at the bottom of the cavity more than uncovered cavities. Therefore, future optimization of the cavity geometry should start with a covered cavity. The present work suggests that the propagation of the pressure fluctuations into a covered cavity can be simplified by solving only the wave equation. This may enable optimization of cavity shape and wall material, with affordable computational costs. However, the very-large eddy simulation using the lattice Boltzmann method is capable of simulating the propagation of the TBL pressure fluctuations into a cavity and therefore is suitable for evaluating future cavity designs, to improve the attenuation of the turbulent boundary layer pressure fluctuations. The computational method used in this study may also apply to cavity design studies at higher Mach numbers when compressible effects become dominant, which would apply to improving the design of microphone cavities for direct noise measurements on aircraft skins.

ACKNOWLEDGMENTS

The research is part of the NWO-TTW THAMES (Towards High-Reynolds Airfoil self-noise MEasurementS) project, with Grant No. 15215. The authors would like to thank the users of the project, for their valuable insight. The authors thank Christopher Teruna and Leandro Rego, for their assistance with the computational tools.

AUTHOR DECLARATIONS

Conflict of Interest

The authors have no conflicts to disclose.

Author Contributions

Hugo Filipe Mourão Bento: Formal analysis (equal); Investigation (equal); Methodology (equal); Validation (equal); Visualization (equal); Writing – original draft (equal); Writing – review & editing (equal). **Colin Paul vanDercreek:** Formal analysis (equal); Investigation (equal); Methodology (equal); Validation (equal); Visualization (equal); Writing – original draft (equal); Writing – review & editing (equal). **Francesco Avallone:** Funding acquisition (equal); Methodology (equal); Supervision (equal); Writing – review & editing (equal). **Daniele Ragni:** Funding acquisition (equal); Supervision (equal); Writing – review & editing (equal). **Mirjam Snellen:** Funding acquisition (equal); Supervision (equal); Writing – review & editing (equal).

DATA AVAILABILITY

The data that support the findings of this study are available from the corresponding authors upon reasonable request.

APPENDIX: DOMAIN AND LATTICE VARIABLE RESOLUTION REGIONS

We show in Table V the dimensions of the domain and of the lattice VR regions.

TABLE V. Dimensions of the domain and of the lattice VR regions. Dimensions shown in cm ($L_{\text{Cylindrical}} = 1$ cm).

	Cylindrical		Countersunk		Conical	
Test case	Uncovered	Covered	Uncovered	Covered	Uncovered	Covered
Domain height	136	136	136	136	136	136
Domain length	300	300	300	300	300	300
Domain width	5.12	5.12	5.12	5.12	11.52	7.68
VR5 height	12.08	12.08	12.08	12.08	21.68	21.72
VR4 height	5.68	5.68	5.68	5.68	15.28	15.32
VR3 height	2.48	2.48	2.48	2.48	2.48	2.52
VR2 height	0.88	0.88	0.88	0.88	0.88	0.92
VR1 height	0.08	0.08	0.08	0.08	0.08	0.12
VR1 length	200	200	200	200	200	200
VR0 height	0.08	0.08	0.08	0.08	0.08	0.08
VR0 diameter	1.16	1.16	1.76	1.76	4.66	4.66
VR0 cell size	0.008	0.008	0.008	0.008	0.01	0.01
Porous medium thickness	×	0.015	×	0.015	×	0.03
VR (−1) thickness	×	0.128	×	0.128	×	0.128
VR (−2) thickness	×	0.032	×	0.032	×	×

REFERENCES

[1]J. Rossiter, "Wind-tunnel experiments on the flow over rectangular cavities at subsonic and transonic speeds," Technical Report No. 64037 (Aeronautical Research Council, 1964).
[2]P. J. W. Block, "Noise response of cavities of varying dimensions at subsonic speeds," Technical Report No. D-8351 (NASA, 1976).
[3]D. Rockwell and E. Naudascher, "Self-sustained oscillations of impinging free shear layers," Annu. Rev. Fluid Mech. **11**, 67–94 (1979).
[4]H. Yokoyama and C. Kato, "Fluid-acoustic interactions in self-sustained oscillations in turbulent cavity flows. I. Fluid-dynamic oscillations," Phys. Fluids **21**, 105103 (2009).
[5]P. Wang, Y. Deng, and Y. Liu, "Vortex-excited acoustic resonance in channel with coaxial side-branches: Vortex dynamics and aeroacoustic energy transfer," Phys. Fluids **30**, 125104 (2018).
[6]Y. W. Ho and J. W. Kim, "A wall-resolved large-eddy simulation of deep cavity flow in acoustic resonance," J. Fluid Mech. **917**, A17 (2021).
[7]C. W. Rowley, T. Colonius, and A. J. Basu, "On self-sustained oscillations in two-dimensional compressible flow over rectangular cavities," J. Fluid Mech. **455**, 315–346 (2002).
[8]L. Larchevêque, P. Sagaut, I. Mary, O. Labbé, and P. Comte, "Large-eddy simulation of a compressible flow past a deep cavity," Phys. Fluids **15**, 193–210 (2003).
[9]F. R. Verdugo, A. Guitton, and R. Camussi, "Experimental investigation of a cylindrical cavity in a low Mach number flow," J. Fluids Struct. **28**, 1–19 (2012).
[10]F. Scarano, M. C. Jacob, R. Gojon, X. Carbonneau, and E. R. Gowree, "Modification of a turbulent boundary layer by circular cavities," Phys. Fluids **34**, 065134 (2022).
[11]C. Haigermoser, F. Scarano, and M. Onorato, "Investigation of the flow in a circular cavity using stereo and tomographic particle image velocimetry," Exp. Fluids **46**, 517–526 (2009).
[12]S. A. Elder, T. M. Farabee, and F. C. Demetz, "Mechanisms of flow-excited cavity tones at low Mach number," J. Acoust. Soc. Am. **72**, 532 (1982).
[13]A. T. D. Jong, Ph.D. thesis, Faculty of Aerospace Engineering, 2012.
[14]B. Ruck and B. Makiola, "Flow separation over the inclined step," in *Physics of Separated Flows–Numerical, Experimental, and Theoretical Aspects* (Springer, 1993), pp. 47–55.
[15]O. Marsden, C. Bailly, C. Bogey, and E. Jondeau, "Investigation of flow features and acoustic radiation of a round cavity," J. Sound Vib. **331**, 3521–3543 (2012).
[16]M. Hiwada, T. Kawamura, I. Mabuchi, and M. Kumada, "Some characteristics of flow patten and heat transfer past a circular cylindrical cavity," Bull. JSME **26**, 1744–1752 (1983).
[17]O. Marsden, C. Bogey, and C. Bailly, "Investigation of flow features around shallow round cavities subject to subsonic grazing flow," Phys. Fluids **24**, 125107 (2012).
[18]P. W. McCarthy and A. Ekmekci, "Flow features of shallow cylindrical cavities subject to grazing flow," Phys. Fluids **34**, 027115 (2022).
[19]A. Rona, "The acoustic resonance of rectangular and cylindrical cavities," J. Algorithms Comput. Technol. **1**, 329–356 (2007).
[20]M. Grottadaurea and A. Rona, "Noise sources from a cylindrical cavity," AIAA Paper No. 2007-3723, 2007.
[21]Y. Yang, D. Rockwell, K. Lai-Fook Cody, and M. Pollack, "Generation of tones due to flow past a deep cavity: Effect of streamwise length," J. Fluids Struct. **25**, 364–388 (2009).
[22]L. F. East, "Aerodynamically induced resonance in rectangular cavities," J. Sound Vib. **3**, 277–287 (1966).
[23]M. L. Pollack, "Flow-induced tones in side-branch pipe resonators," J. Acoust. Soc. Am. **67**, 1153 (1980).
[24]V. Fleury, L. Coste, R. Davy, A. Mignosi, C. Cariou, and J.-M. M. Prosper, "Optimization of microphone array wall mountings in closed-section wind tunnels," AIAA J. **50**, 2325–2335 (2012).
[25]S. Jaeger, W. Horne, and C. Allen, "Effect of surface treatment on array microphone self-noise," in *6th AIAA/CEAS Aeroacoustics Conference and Exhibit, Aeroacoustics Conferences* (American Institute of Aeronautics and Astronautics, Lahaina, HI, 2000).
[26]C. P. VanDercreek, A. Amiri-Simkooei, M. Snellen, and D. Ragni, "Experimental design and stochastic modeling of hydrodynamic wave propagation within cavities for wind tunnel acoustic measurements," Int. J. Aeroacoust. **18**, 752–779 (2019).
[27]C. VanDercreek, R. Merino-Martínez, P. Sijtsma, and M. Snellen, "Evaluation of the effect of microphone cavity geometries on acoustic imaging in wind tunnels," Appl. Acoust. **181**, 108154 (2021).
[28]C. Teruna, F. Manegar, F. Avallone, D. Ragni, D. Casalino, and T. Carolus, "Noise reduction mechanisms of an open-cell metal-foam trailing edge," J. Fluid Mech. **898**, A18 (2020).
[29]P. L. Bhatnagar, E. P. Gross, and M. Krook, "A model for collision processes in gases. I. Small amplitude processes in charged and neutral one-component systems," Phys. Rev. **94**, 511–525 (1954).
[30]C. M. Teixeira, "Incorporating turbulence models into the lattice-Boltzmann method," Int. J. Mod. Phys. C **9**, 1159–1175 (1998).
[31]V. Yakhot and S. A. Orszag, "Renormalization group analysis of turbulence. I. Basic theory," J. Sci. Comput. **1**, 3–51 (1986).
[32]C. Teruna, L. Rego, F. Avallone, D. Ragni, and D. Casalino, "Applications of the multilayer porous medium modeling approach for noise mitigation," J. Aerosp. Eng. **34**, 04021074 (2021).
[33]C. Teruna, F. Manegar, F. Avallone, D. Casalino, D. Ragni, A. Rubio-Carpio, and T. Carolus, "Numerical analysis of metal-foam application for trailing edge noise reduction," AIAA Paper No. 2019-2650, 2019.
[34]G. E. Elsinga and J. Westerweel, "Tomographic-PIV measurement of the flow around a zigzag boundary layer trip," Exp. Fluids **52**, 865–876 (2012).
[35]R. Merino-Martinez, W. van der Velden, F. Avallone, and D. Ragni, "Acoustic measurements of a DU96-W-180 airfoil with flow-misaligned serrations at a high Reynolds number in a closed-section wind tunnel," in 7th International Conference on Wind Turbine Noise Rotterdam (2017).
[36]G. M. Corcos, "The structure of the turbulent pressure field in boundary-layer flows," J. Fluid Mech. **18**, 353–378 (1964).
[37]R. Merino-Martínez, A. Rubio Carpio, L. T. Lima Pereira, S. van Herk, F. Avallone, D. Ragni, and M. Kotsonis, "Aeroacoustic design and characterization of the 3D-printed, open-jet, anechoic wind tunnel of Delft University of Technology," Appl. Acoust. **170**, 107504 (2020).
[38]T. J. Mueller, *Experimental Fluid Mechanics* (Springer, Berlin, 2002).
[39]A. Rubio Carpio, R. Merino Martínez, F. Avallone, D. Ragni, M. Snellen, and S. van der Zwaag, "Experimental characterization of the turbulent boundary layer over a porous trailing edge for noise abatement," J. Sound Vib. **443**, 537–558 (2019).
[40]S. Luesutthiviboon, D. Ragni, F. Avallone, and M. Snellen, "An alternative permeable topology design space for trailing-edge noise attenuation," Int. J. Aeroacoust. **20**, 221–253 (2021).
[41]X. Gloerfelt and J. Berland, "Turbulent boundary-layer noise: Direct radiation at Mach number 0.5," J. Fluid Mech. **723**, 318–351 (2013).
[42]J. H. M. Ribeiro and W. R. Wolf, "Identification of coherent structures in the flow past a NACA0012 airfoil via proper orthogonal decomposition," Phys. Fluids **29**, 085104 (2017).
[43]M. A. Mendez, M. Balabane, and J. M. Buchlin, "Multi-scale proper orthogonal decomposition of complex fluid flows," J. Fluid Mech. **870**, 988–1036 (2019).
[44]D. Ninni and M. A. Mendez, "MODULO: A software for multiscale proper orthogonal decomposition of data," SoftwareX **12**, 100622 (2020).
[45]L. Eça and M. Hoekstra, "Discretization uncertainty estimation based on a least squares version of the grid convergence index," in *Proceedings of the Second Workshop on CFD Uncertainty Analysis* (Instituto Superior Tecnico, Lisbon, 2006).
[46]S. Ghaemi and F. Scarano, "Turbulent structure of high-amplitude pressure peaks within the turbulent boundary layer," J. Fluid Mech. **735**, 381–426 (2013).
[47]I. Marusic and G. J. Kunkel, "Streamwise turbulence intensity formulation for flat-plate boundary layers," Phys. Fluids **15**, 2461–2464 (2003).
[48]Q. Zhang and D. J. Bodony, "Numerical investigation of a honeycomb liner grazed by laminar and turbulent boundary layers," J. Fluid Mech. **792**, 936–980 (2016).
[49]H. Schlichting and K. Gersten, *Boundary-Layer Theory*, 9th ed. (Springer, 1987).

[50]K. Mori, H. Imanishi, Y. Tsuji, T. Hattori, M. Matsubara, S. Mochizuki, M. Inada, and T. Kasiwagi, "Direct total skin-friction measurement of a flat plate in zero-pressure-gradient boundary layers," Fluid Dyn. Res. **41**, 021406 (2009).
[51]L. T. Lima Pereira, D. Ragni, F. Avallone, and F. Scarano, "Pressure fluctuations from large-scale PIV over a serrated trailing edge," Exp. Fluids **61**, 71 (2020).
[52]S. Pröbsting, M. Tuinstra, and F. Scarano, "Trailing edge noise estimation by tomographic particle image velocimetry," J. Sound Vib. **346**, 117–138 (2015).
[53]J. Jeong and F. Hussain, "On the identification of a vortex," J. Fluid Mech. **285**, 69–94 (1995).
[54]C. P. VanDercreek, F. Avallone, D. Ragni, and M. Snellen, "Simulating the acoustic response of cavities to improve microphone array measurements in closed test section wind tunnels," J. Acoust. Soc. Am. **151**, 322 (2022).
[55]G. P. Scavone, "An acoustic analysis of single-reed woodwind instruments with an emphasis on design and performance issues and digital waveguide modeling techniques," Ph.D. thesis (Stanford University, 1997).
[56]W. K. Blake, "Essentials of turbulent wall pressure fluctuations," in *Mechanics of Flow-Induced Sound and Vibration* (Elsevier, 2017), Vol. 2, pp. 81–177.
[57]L. Larchevêque, P. Sagaut, T. H. Lê, and P. Comte, "Large-eddy simulation of a compressible flow in a three-dimensional open cavity at high Reynolds number," J. Fluid Mech. **516**, 265–301 (2004).
[58]S. W. Rienstra, *Fundamentals of Duct Acoustics* (Eindhoven University of Technology, 2015), pp. 1–50.
[59]*Handbook of Mathematical Functions*, edited by M. Abramowitz and I. A. Stegun (National Bureau of Standards, Washington, DC, 1964).
[60]C. P. VanDercreek, P. Sijtsma, M. Snellen, D. Ragni, F. Avallone, and D. G. Simons, "Deterministic model of acoustic wave propagation in a cavity," in *25th AIAA/CEAS Aeroacoustics Conference, Aeroacoustics Conferences* (American Institute of Aeronautics and Astronautics, 2019).